



## Injection of meteoric phosphorus into planetary atmospheres

Juan Diego Carrillo-Sánchez<sup>a</sup>, David L. Bones<sup>a</sup>, Kevin M. Douglas<sup>a</sup>, George J. Flynn<sup>b</sup>, Sue Wirick<sup>c</sup>, Bruce Fegley Jr.<sup>d</sup>, Tohru Araki<sup>e</sup>, Burkhard Kaulich<sup>e</sup>, John M.C. Plane<sup>a,\*</sup>

<sup>a</sup> School of Chemistry, University of Leeds, Woodhouse Lane, Leeds, LS2 9JT, UK

<sup>b</sup> State University of New York at Plattsburgh, Department of Physics, 101 Broad Street, Plattsburgh, NY, 12901, USA

<sup>c</sup> Focused Beam Enterprises, Westhampton, NY, 11977, USA

<sup>d</sup> Planetary Chemistry Laboratory, Department of Earth & Planetary Sciences and McDonnell Center for the Space Sciences, Washington University, St Louis, MO, 63130, USA

<sup>e</sup> Diamond Light Source Ltd, Harwell Science & Innovation Campus, Didcot, OX11 0DE, UK

### ARTICLE INFO

#### Keywords:

Cosmic dust  
Planetary atmospheres  
Ablation  
Phosphorus thermodynamics  
Zodiacal cloud

### ABSTRACT

This study explores the delivery of phosphorus to the upper atmospheres of Earth, Mars, and Venus via the ablation of cosmic dust particles. Micron-size meteoritic particles were flash heated to temperatures as high as 2900 K in a Meteor Ablation Simulator (MASI), and the ablation of PO and Ca recorded simultaneously by laser induced fluorescence. Apatite grains were also ablated as a reference. The speciation of P in anhydrous chondritic porous Interplanetary Dust Particles was made by K-edge X-ray absorption near edge structure (XANES) spectroscopy, demonstrating that P mainly occurs in phosphate-like domains. A thermodynamic model of P in a silicate melt was then developed for inclusion in the Leeds Chemical Ablation Model (CABMOD). A Regular Solution model used to describe the distribution of P between molten stainless steel and a multicomponent slag is shown to provide the most accurate solution for a chondritic-composition, and reproduces satisfactorily the PO ablation profiles observed in the MASI. Meteoritic P is moderately volatile and ablates before refractory metals such as Ca; its ablation efficiency in the upper atmosphere is similar to Ni and Fe. The speciation of evaporated P depends significantly on the oxygen fugacity, and P should mainly be injected into planetary upper atmospheres as PO<sub>2</sub>, which will then likely undergo dissociation to PO (and possibly P) through hyperthermal collisions with air molecules. The global P ablation rates are estimated to be 0.017 t d<sup>-1</sup> (tonnes per Earth day), 1.15 × 10<sup>-3</sup> t d<sup>-1</sup> and 0.024 t d<sup>-1</sup> for Earth, Mars and Venus, respectively.

### 1. Introduction

Phosphorus, P, is one of the key biological elements, with compounds of phosphorus appearing profusely in living systems where they play a major role in many fundamental biochemical functions, including replication, information transfer, and metabolism (Maciá, 2005). Together with the other main biogenic elements, H, C, O, N, and S, P is present in all known lifeforms. Despite the biological importance of P, it is relatively scarce on a cosmic scale, with an elemental abundance of  $3.4 \times 10^{-7}$  relative to H in the Sun's atmosphere (Lodders, 2003). Ortho-phosphate (oxidation state +5), is the dominant form of inorganic P on the Earth's surface. However, the low water solubility and reactivity of such P(V) salts mean they have a poor bioavailability. Indeed, low concentrations of dissolved P in water on the Earth often make it a limiting reagent in many ecosystems, as well as giving rise to the 'phosphorus problem' in the

origin or life (Redfield, 1958; Schwartz, 2006).

More reduced forms of P (oxidation state  $\leq +3$ ) are, however, far more soluble, and as such have an improved bioavailability. One possible source of these reduced forms of P is from extraterrestrial material that fell to Earth during the heavy bombardment period. Pasek (2008) investigated the direct delivery of P to the surface of the Earth in meteorites, which might then undergo processing through aqueous phase chemistry. In their study, they demonstrate how phosphides, present as the mineral schreibersite in Pallasite iron nickel meteorites, can be oxidized in water to form several prebiotic P species. However, iron nickel meteorites only make up around 1% of the total annual mass influx of exogenous material entering the Earth's atmosphere, with interplanetary dust particles (IDPs) making up the other 99% (Plane et al., 2017). An alternative route to reduced forms of P has been proposed in the form of atmospheric processing of vaporized P atoms, which enter planetary

\* Corresponding author.

E-mail address: [j.m.c.plane@leeds.ac.uk](mailto:j.m.c.plane@leeds.ac.uk) (J.M.C. Plane).

<https://doi.org/10.1016/j.pss.2020.104926>

Received 15 November 2019; Received in revised form 9 February 2020; Accepted 31 March 2020

Available online 8 April 2020

0032-0633/© 2020 The Authors. Published by Elsevier Ltd. This is an open access article under the CC BY license (<http://creativecommons.org/licenses/by/4.0/>).

atmospheres via meteoric ablation of IDPs (Douglas et al., 2019). These vaporized P atoms will undergo chemical processing to form a variety of compounds in which P may exist in different oxidation states due to the presence of both reducing and oxidizing agents in these atmospheres. Thus, an understanding of the ablation of P is crucial for understanding the fate of exogenous P and its impact in the atmosphere and at the surface.

The first objective of the present study was to explore the differential ablation of phosphorus using the Meteor Ablation Simulator (MASI) (Bones et al., 2016; Gómez-Martín et al., 2017), an experimental setup that detects the evaporating metals from meteoritic samples by Laser-Induced Fluorescence (LIF). The second objective was to develop a new version of the MAGMA thermodynamic module (Fegley and Cameron, 1987) to model the evaporation of phosphorus by comparing different thermodynamic models of P and its oxides (Suito et al., 1981; Ban-Ya, 1993; Turkdogan, 2000; Jung and Hudon, 2012). MAGMA was then implemented within the new version of CABMOD, and the phosphorus ablation profiles predicted by CABMOD were compared and validated with the corresponding experimental profiles measured by MASI.

In order to develop the P thermodynamic module in MAGMA, the major speciation of P in IDPs needs to be known. The third objective of this study was therefore to determine the P speciation in small (~15 µm) anhydrous chondritic porous interplanetary dust particles (CP IDPs). These measurements were made by K-edge X-ray absorption near edge structure (XANES) spectroscopy. This spectroscopic technique, coupled with the scanning X-ray microscope (SXM) on the I08 beamline of the Diamond Light Source, allows the spatial distribution and speciation of phosphorus in the IDPs studied to be determined. These CP IDPs offer some of the best preserved samples of primitive presolar materials and the original condensates of the solar protoplanetary disk (Ishii et al., 2008). As such, the mineralogy of these particles offers insights into the condensation processes occurring in such protoplanetary disks, as well as a test for models predicting these processes. Many of these equilibrium condensation models predict phosphorus condensing in its reduced form, as a phosphide in the mineral schreibersite (Lodders, 2003).

The final objective, achieved by combining CABMOD with an astronomical model of dust sources and evolution in the solar system (Nesvorný et al., 2011; Carrillo-Sánchez et al., 2020), was to estimate the injection rate profiles of phosphorus in the atmospheres of Earth, Mars, and Venus, in order to determine the global mass influx accreted by these planets.

## 2. Experimental methods and thermodynamic modelling

### 2.1. The meteoric ablation simulator (MASI)

As described previously (Bones et al., 2016; Gómez-Martín et al., 2017), particles were flash heated in the Meteoric Ablation simulator (MASI) chamber to temperatures as high as 2900 K at pressures of about 15 Pa (in N<sub>2</sub>). The simulator consists of a stainless steel chamber with a tungsten filament mounted inside. The filament is 40 mm long, 1 mm wide and 0.025 mm thick. The relative concentration of the diatomic molecule PO was measured by time-resolved laser induced fluorescence (LIF) at 246.27 nm (PO(A<sup>2</sup>Σ<sup>+</sup> – X<sup>2</sup>Π (ν', ν'' 0, 0)) (Sausa et al., 1986)). The ablation of Ca was observed simultaneously by LIF at 422.65 nm (Ca(4<sup>1</sup>P – 4<sup>1</sup>S)). The laser beams were produced by Sirah Cobra dye lasers pumped at 355 nm by Nd-YAG lasers. For PO LIF, where the dye laser output at 492 nm was doubled to 246 nm and the PO transition is relatively weak, a Continuum Surelite II Nd-YAG operating at 10 Hz was used; in this case, time resolution was sacrificed for LIF signal strength. For Ca, a Litron TRL-Nano 50–250 Nd:YAG was used operating at 250 Hz.

The temperature of the filament was measured by a pyrometer (System 4 Ratio Thermometer Land Instruments) capable of measurements between 1273 K and 2873 K with 15 ms time resolution. In previous work, a feedback algorithm was used to produce controlled temperature

**Table 1**

Samples analysed by SXM/XANES spectroscopy.

Sample	Short name	No. P hotspot regions	White line position (eV)
Apatite standard	Apatite	2	2152.7
Orgueil meteorite	Orgueil	2	2152.7
L2009 E6	E6	5	2152.3
U2073A – 5ab.1	5ab.1	6	2152.3
L2009 E2	E2	3	2152.4
U2073A 5ab.3	5ab.3	4	2152.4
U20797 A19	A19	0	–

profiles simulating atmospheric entry. In the present study the current was linearly ramped. While this resulted in somewhat non-linear temperature profiles, it extended filament life and avoided rapid oscillations at each end of the pyrometer measurement range, therefore extending the useful temperature range. This procedure also avoided a problem with inaccurate temperature measurements caused by particles moving through the pyrometer focus (Bones et al., 2016). This problem was evident as dips in the temperature profile, resulting in temperature spikes as the heating algorithm tried to compensate. The temperature profiles were approximated as a linear function by fitting a straight line from the point at which  $T = 1700$  K to the maximum temperature of the profile (typically 2800 K). This allowed direct comparison with CABMOD output whilst avoiding the dips in apparent temperature from moving particles.

Powdered samples were prepared by grinding terrestrial minerals or meteorites in an agate mortar and pestle, then separating them into size bins with a sieve (Endecott Test Sieve). For a reference mineral, we chose apatite, a phosphorus-rich mineral with formula Ca<sub>10</sub>(PO<sub>4</sub>)<sub>6</sub>(OH,F,Cl)<sub>2</sub>. The apatite sample was commercially obtained from Alfa Aesar. As previously, the terrestrial meteorite sample was from the Allende meteorite, a carbonaceous chondrite classified as CV3. Although our previous Scanning Electron Microscope-Energy Dispersive X-ray (SEM-EDX) analyses of Allende did not show the presence of any phosphorus (Gómez-Martín et al., 2017; Bones et al., 2019), the original analysis of Allende (Clarke et al., 1971) gave a value of 0.24 wt% of P<sub>2</sub>O<sub>5</sub> (see Table S1 in the Supporting Information), equivalent to 0.10 wt% P. Subsequent analyses agree with this value, which would be below the detection limit for our SEM-EDX analyses.

A small amount of the prepared sample was placed on the tungsten filament. The sample was heated to around 2800 K by linearly ramping the current flowing through the filament between 1.5 and 5 A. As the filament aged, the maximum current was reduced to keep the maximum temperature at around 2873 K, the upper limit of the pyrometer range. While the temperature response from the filament was initially non-linear, above temperatures of about 1600 K, an approximately linear temperature response was observed. P is expected to ablate as PO or PO<sub>2</sub> (Pasek, 2015). PO was chosen as the ablation product that was most likely detectable by LIF. During the course of the experiments, we attempted to detect PO<sub>2</sub> (at 282 nm) and the excited state <sup>2</sup>P state of atomic P (at 253.6 nm). Excited P atoms were observed, but the triatomic PO<sub>2</sub> molecule was not detected, which we attribute to the greater difficulty in detecting larger molecules by LIF (triatomic molecules typically have smaller cross sections and smaller resonance fluorescence yields compared to diatomic molecules and atoms such as PO and P(<sup>2</sup>P)).

### 2.2. Spatial distribution and speciation of phosphorus in IDPs by XANES spectroscopy

For this study we analysed five ultra-microtomed thin sections from four CP IDPs, together with a powdered sample of the Orgueil meteorite and a powdered piece of Apatite standard (Table 1). The IDPs were provided to us by the Cosmic Dust Curatorial Facility at the NASA Johnson Space Centre. They were chosen from a set of IDPs characterized

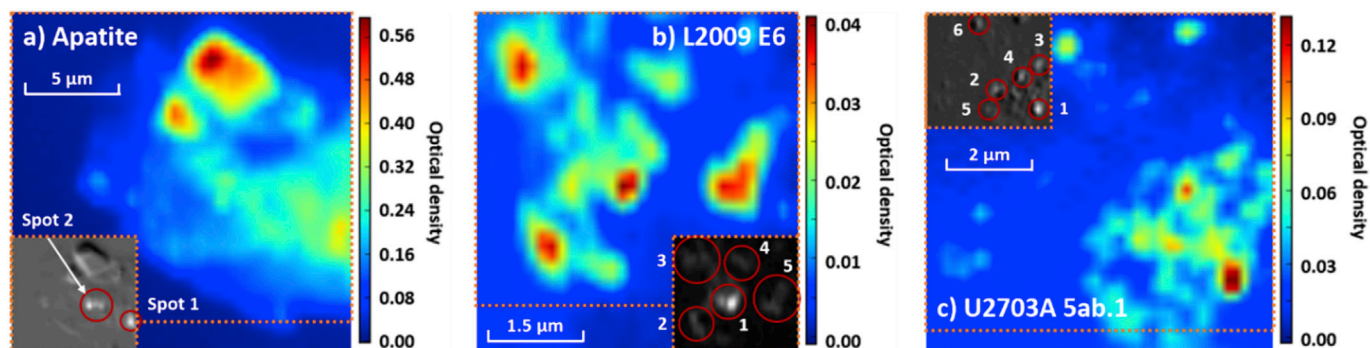


Fig. 1. Optical density maps and differential maps to identify P hotspot regions (insets) of the Apatite sample slice (a), and of the IDP slices L2009 E6 (b) and U2703A 5ab.1 (c).

by TEM and known to be anhydrous CP-IDPs, which had previously been studied for organics by C-XANES (Flynn et al., 2013). The thin slices were prepared using a technique traditionally employed to prepare samples for transmission electron microscopes, in which a sharp diamond knife is forced over the sample to produce slices between 70 and 100 nm thick. Such thin slices were required for initial X-ray transmission carbon K-edge analyses of these IDPs; for P, sections could be as thick as a micron, with approximately 70% transmission at 2150 eV for apatite. Further details regarding the preparation of the thin sample slices can be found in Flynn et al. (2003). The powdered samples were prepared following the technique described by Wirick et al. (2006), where powdered samples are suspended onto a droplet of clean water and transferred to a formvar backed, copper TEM by touching the grid to the surface of the droplet.

The sample slices were examined using the scanning X-ray microscope (SXM) endstation on the I08 beamline at the Diamond Light Source (DLS). This beamline uses a zone plate to focus coherent X-rays down to an approximately 100 nm spot. The X-ray transmission through the sample is recorded by a detector located behind the sample. Imaging is achieved by raster scanning the sample through the fixed beam at a selected X-ray energy. Image stacks of particles were collected at energies between 2133 and 2183 eV, across the phosphorus *K* absorption edge. For a typical image stack, steps of 0.2 eV were employed over the critical energy range between 2143 and 2156 eV, where distinctive molecular features involving P occur, while steps of 1 eV were employed at the higher and lower energy ranges. The image stacks were aligned using Mantis, and optical density maps of the X-ray transmission across the sample produced (see Fig. 1). XANES spectra from single spots or regions can then be extracted. To identify phosphorus hotspots in the samples, a number of images in the pre-edge spectral region, and a number of images over the peak, were averaged, and a differential map produced by subtracting one from the other. Areas of high P concentration are then clearly visible in these differential maps (white spots in insets in Fig. 1), and XANES spectra of the high P regions extracted. P hotspots were identified in all but one (U20797 A19) of the IDP samples (Table 1). Indeed, it should be noted that for the apatite sample, and for IDP fragments L2009E6, U2073A-5AB.1, and U2073A-5AB.3, there was evidence of phosphorus across the entire sample, with a few highly concentrated areas of P.

The energy scale of the extracted XANES spectra were calibrated using the position of the principal *K*-edge peak (termed the white line) in the Apatite standard. While literature values of the position of the white line in apatite can vary by up to an eV (Brandes et al., 2007; Ingall et al., 2011; Li et al., 2015), we have chosen to use the value of 2152.7 eV (Kim et al., 2015b) as given by the European Synchrotron Radiation Facility (ESRF), which contains a database of organic and inorganic phosphorus XANES data. Where literature values of the white line of Apatite do differ we have used the value of 2152.7 eV to adjust their peak positions.

### 2.3. The Chemical Ablation Model (CABMOD)

To model the ablation of P we use the CABMOD model, which includes a detailed description of the physical and chemical processes of meteoric ablation in a planetary upper atmosphere (Vondrak et al., 2008; Carrillo-Sánchez et al., 2020). CABMOD has been widely tested with experimental time-resolved simulations using the MASI system (Gómez-Martín et al., 2017; Bones et al., 2018, 2019), and it has successfully reproduced events associated with meteoric ablation such as the strong E region ionization associated with the 2002 Leonids (Pellinen-Wannberg et al., 2014), the MAVEN-IUVS observations of Mg in the Mars atmosphere caused by comet Siding Spring's encounter (Schneider et al., 2015; Crismani et al., 2018), and modeling the altitude distribution of Meteor Head Echoes observed by HPLA radars (Janches et al., 2017; Swarnalingam et al., 2019). CABMOD was recently updated with a multiphase treatment to account for the ablation of both molten-bulk silicate and the Fe–Ni metal domains present in IDPs (Bones et al., 2019; Carrillo-Sánchez et al., 2020), assuming that silicate and metal phases are completely immiscible (Hutchinson, 2007) due to density differences: 2200 kg m<sup>-3</sup> for the silicate bulk (Consolmagno et al., 2008) and an average density of 4710 kg m<sup>-3</sup> for pyrrhotite and pentlandite inclusions (Bones et al., 2019). Consequently, CABMOD estimates the vapour pressures of the different metals from both MAGMA (Fegley and Cameron, 1987; Schaefer and Fegley, 2005) and Fe–Ni thermodynamic modules, which are called separately when the respective melting point of each phase is reached (Carrillo-Sánchez et al., 2020). These melting points are ~1760 K for Fe–Ni metal grains (Swartzendruber et al., 1991), and ~1800 K for an olivine phase with a chondritic Fe:Mg ratio of 0.84 (Vondrak et al., 2008).

In meteorites, phosphorus may occur as both phosphates and phosphides. Phosphates are typical of stony meteorites, while phosphides in the form (Fe, Ni)<sub>3</sub>P are mainly present in iron meteorites (Buchwald, 1984). In the Earth, 95.4% of total phosphorus is located in the core, most likely in the form of Fe<sub>3</sub>P (Gu et al., 2014; Pasek et al., 2017), whereas the remaining phosphorus is located in the lithophilic mantle. For the development of CABMOD, we assume that: 1) Phosphorus is mainly oxidized in IDPs, as shown by the P-XANES spectra discussed in Section 3.1, and therefore the thermodynamic data (Section 2.3.1) as well as the different models used to estimate the activity coefficients (Section 2.3.2) refer to the molten oxide P<sub>2</sub>O<sub>5</sub>(l); and 2) Phosphorus diffuses to the silicate phase in the molten particle. In this section we discuss how phosphorus is implemented within the MAGMA thermodynamic module.

#### 2.3.1. Thermodynamic data for P<sub>2</sub>O<sub>5</sub>

The MAGMA thermodynamic model (Fegley and Cameron, 1987; Schaefer and Fegley, 2005) computes the composition of the gas phase in equilibrium with the molten silicate bulk using a multicomponent chemical equilibrium solution (Hastie et al., 1982, 1984; Hastie and

**Table 2**

Thermodynamic data for the equilibrium constant  $\log(K)$ : 1. Pure liquid oxide vaporization to constituent atoms; 2. Formation of phosphorus gases included in the vaporization calculations; and 3. Relating the activities of pseudo-species.

Reaction	$\log(K)$	References
Thermodynamic data for pure liquid oxide to constituent atoms		
$\text{SiO}_2(l) \rightleftharpoons \text{Si}(g) + 2\text{O}(g)$	$21.13 - 94311.0/T$	(Stull and Prophet, 1971; Chase et al., 1985)
$\text{MgO}(l) \rightleftharpoons \text{Mg}(g) + \text{O}(g)$	$12.56 - 46992.0/T$	(Stull and Prophet, 1971; Chase et al., 1985)
$\text{FeO}(l) \rightleftharpoons \text{Fe}(g) + \text{O}(g)$	$12.06 - 44992.0/T$	(Stull and Prophet, 1971; Chase et al., 1985)
$\text{CaO}(l) \rightleftharpoons \text{Ca}(g) + \text{O}(g)$	$11.88 - 49586.0/T$	(Stull and Prophet, 1971; Chase et al., 1985)
$\text{Al}_2\text{O}_3(l) \rightleftharpoons 2\text{Al}(g) + 3\text{O}(g)$	$35.83 - 153255.0/T$	Chase et al. (1985)
$\text{TiO}_2(l) \rightleftharpoons \text{Ti}(g) + 2\text{O}(g)$	$4.31 - 2101/T$	(Stull and Prophet, 1971; Chase et al., 1985)
$\text{Na}_2\text{O}(l) \rightleftharpoons 2\text{Na}(g) + \text{O}(g)$	$15.56 - 40286.0/T$	(Stull and Prophet, 1971; Chase et al., 1985)
$\text{K}_2\text{O}(l) \rightleftharpoons 2\text{K}(g) + \text{O}(g)$	$15.21 - 36404.0/T$	(Glushko et al., 1978-1982; Chase et al., 1985)
$\text{P}_2\text{O}_5(l) \rightleftharpoons 2\text{P}(g) + 5\text{O}(g)$	$51.61 - 176527.5/T$	(Hultgren et al., 1973; Chase et al., 1985; Jung and Hudon, 2012)
$\text{P}_2\text{O}_5(l) \rightleftharpoons 2\text{P}(g) + 5\text{O}(g)$	$53.28 - 178570.3/T$	(Hultgren et al., 1973; Chase et al., 1985; Turkdogan, 2000)
Thermodynamic data for formation of phosphorus gases included in the vaporization calculations		
$\frac{1}{2}\text{O}_2(g) \rightleftharpoons \text{O}(g)$	$3.47 - 13282.0/T$	Chase et al. (1985)
$\text{P}(l) \rightleftharpoons \text{P}(g)$	$6.19 - 16749.1/T$	Robie et al. (1979)
$\text{P}(l) + \frac{1}{2}\text{O}_2(g) \rightleftharpoons \text{PO}(g)$	$2.87 + 1032.5/T + 1.88 \times 10^6/T^2 + 1.96 \times 10^9/T^3 + 9.04 \times 10^{11}/T^4 + 1.99 \times 10^{14}/T^5 + 1.70 \times 10^{16}/T^6$	(Robie et al., 1979; Chase et al., 1985)
$\text{P}(l) + \text{O}_2(g) \rightleftharpoons \text{PO}_2(g)$	$-8.21 \times 10^{-3} + 16280.0/T$	(Robie et al., 1979; Chase et al., 1985)
Thermodynamic data for the activities of phosphorus pseudo-species		
$3\text{CaO}(l) + \text{P}_2\text{O}_5(l) \rightleftharpoons \text{Ca}_3(\text{PO}_4)_2(s)$	$3.01 + 33839.1/T + 8.57 \times 10^6/T^2 - 1.43 \times 10^9/T^3$	(Robie et al., 1979; Chase et al., 1985; Jung and Hudon, 2012)
$\frac{1}{2}\text{Al}_2\text{O}_3(l) + \frac{1}{2}\text{P}_2\text{O}_5(l) \rightleftharpoons \text{AlPO}_4(s)$	$3.91 + 2598.1/T + 2.80 \times 10^6/T^2 - 4.17 \times 10^9/T^3$	(Robie et al., 1979; Chase et al., 1985; Jung and Hudon, 2012)
$3\text{CaO}(l) + \text{P}_2\text{O}_5(l) \rightleftharpoons \text{Ca}_3(\text{PO}_4)_2(s)$	$4.68 + 31796.3/T + 8.57 \times 10^6/T^2 - 1.43 \times 10^9/T^3$	(Robie et al., 1979; Chase et al., 1985; Turkdogan, 2000)
$\frac{1}{2}\text{Al}_2\text{O}_3(l) + \frac{1}{2}\text{P}_2\text{O}_5(l) \rightleftharpoons \text{AlPO}_4(s)$	$4.75 + 1576.7/T + 2.80 \times 10^6/T^2 - 4.17 \times 10^9/T^3$	(Robie et al., 1979; Chase et al., 1985; Turkdogan, 2000)

Bonnell, 1985, 1986). For this purpose, MAGMA initially assumes an Ideal Mixing of pure molten oxides –  $\text{SiO}_2$ ,  $\text{MgO}$ ,  $\text{FeO}$ ,  $\text{Al}_2\text{O}_3$ ,  $\text{CaO}$ ,  $\text{TiO}_2$ ,  $\text{Na}_2\text{O}$ , and  $\text{K}_2\text{O}$  - with the typical chondritic abundances (Table S1 in the Supporting Information summarizes the composition of a CI-chondrite (Lodders and Fegley, 2011) and CV3 Allende samples (Clarke et al., 1971)). According to MAGMA, the vaporization of a pure molten oxide can be expressed as:



where M represents the metal (Table 2 shows the thermodynamic data for the pure liquid oxides used in MAGMA). MAGMA then assesses the vapour pressure equilibria of all metals and oxygen, solving iteratively a set of non-linear equations that take into account the thermodynamic activities,  $a_i$ , of the metal oxides in a non-ideal solution:

$$a_i = \gamma_i x_i \quad (2)$$

where  $\gamma_i$  is the Raoultian activity coefficient of the oxide metal relative to the pure liquid oxide, and  $x_i$  is the mole fraction of the oxide in the melt. The MAGMA model uses an empirical solution to estimate the activity coefficients of the metal oxides as a function of temperature and concentration. In summary, the unbound metal oxides in the silicate melt are reduced by the formation of complex oxides and pseudo-components that are assumed to mix ideally in the melt. The activities of the oxides in the non-ideal silicate melt are then given by the mole fraction of the unbound oxides in the melt:

$$a_i = x_{oxide}^* \quad (3)$$

where  $x_{oxide}^*$  is the mole fraction of the unbound oxide in the silicate melt. Therefore, the Raoultian activity coefficient can be written as:

$$\gamma_i = \frac{x_{oxide}^*}{x_i} \quad (4)$$

Section 2.3.2 describes in detail the reactions involved in the production of the pseudo-species from  $\text{P}_2\text{O}_5$  and that, therefore, reduce its concentration in the silicate magma.

Thermodynamic properties of  $\text{P}_2\text{O}_5$  have been widely studied because of its use in the metallurgical and glassmaking industries (Ban-Ya, 1993; Jung et al., 2013; Yang et al., 2016; Khadhraoui et al., 2019). In fact, the  $\text{CaO-SiO}_2\text{-MgO-FeO}_n\text{-P}_2\text{O}_5$  system constitutes the basic system present during the steelmaking process, since these components may represent above 90 wt% of all constituents of steelmaking slags (Chen et al., 2013). The JANAF thermochemical tables list the most widely accepted data for solid  $\text{P}_2\text{O}_5$ , even though these datasets refer to the metastable hexagonal phase ( $\text{P}_4\text{O}_{10}$ ) (Chase et al., 1985). Several studies (Richardson and Jeffes, 1948; Turkdogan and Pearson, 1953; Olette and Ancy-Moret, 1963; Turkdogan, 2000; Jung and Hudon, 2012) have reported the Gibbs free energies of formation ( $\Delta G_f^0$ ) of pure liquid  $\text{P}_2\text{O}_5$  for the following reaction:



In the present study, we focus on the most recent estimates from Turkdogan (2000) and Jung and Hudon (2012). Turkdogan (2000) revised his previous estimate for  $\Delta G_f^0$  of the hypothetical pure liquid  $\text{P}_2\text{O}_5$  (Turkdogan and Pearson, 1953) by examining the phosphorus distribution between molten steel and multicomponent slag at three temperatures – 1823, 1873 and 1973 K - and derived the following expression:

$$\Delta G_f^0 = -1,655,500 + 571.0T \text{ (J mol}^{-1}\text{)} \quad (6)$$

More recently, Jung and Hudon (2012) evaluated  $\Delta G_f^0$  assuming its most stable form,  $o\text{-P}_2\text{O}_5$  (orthorhombic, stable up to its melting point at 853 K at atmospheric pressure). This gave:

$$\Delta G_f^0 = -1,616,400 + 539.0T \text{ (J mol}^{-1}\text{)} \quad (7)$$

Note that the values of the standard enthalpies of formation,  $\Delta H_f^0$ , in equations [6] and [7] only differ by 39 kJ mol<sup>-1</sup>, and the standard entropy of formation,  $\Delta S_f^0$ , is only 32 J mol<sup>-1</sup> K<sup>-1</sup> less negative in the later study.

Hultgren et al. (1973) used the experimental results reported by Gingerich (1969), who had studied the dissociation reaction of  $\text{P}_2(g)$

(equation [8]) over the temperature range 1916–2198 K using the Knudsen effusion technique combined with mass spectrometric analysis of the vapour, to determine  $\Delta G_f^0$ :

$$P_2(g) \rightleftharpoons 2P(g) \quad (8)$$

$$\Delta G_f^0 = 504,900 - 123.36T \text{ (J mol}^{-1}\text{)} \quad (9)$$

where equation [9] is widely accepted in the study of the thermodynamic properties of phosphorus and solid binary phosphides (Schlesinger, 2002). Moreover, equation [9] is in good agreement with the estimate of  $\Delta G_f^0$  from the JANAF thermochemical tables (Chase et al., 1985), which evaluated the thermodynamic dataset of  $P_2(g)$  theoretically using the molecular and spectroscopic constants listed by Herzberg (1945):

$$\Delta G_f^0 = 495,230 - 118.91T \text{ (J mol}^{-1}\text{)} \quad (10)$$

As mentioned above, in the present study we provide a comparison between the estimates of the Gibbs free energy of formation of liquid  $P_2O_5$  reported by Turkdogan (2000) and Jung and Hudon (2012). The vaporization of a molten pure oxide in MAGMA needs to be expressed as shown in equation [1], that is, in the case of  $P_2O_5(l)$ :



Therefore, the Gibbs free energy for equation [11] in MAGMA is calculated by combining either equation [6] (Turkdogan, 2000) or equation [7] (Jung and Hudon, 2012) with equation [9] and the JANAF thermochemical data for the dissociation of diatomic  $O_2$  to atomic O (Chase et al., 1985). As a result,  $\Delta G_f^0$  for reaction 11 is

$$\Delta G_f^0 = 342,680 - 1025.9T \text{ (J mol}^{-1}\text{)} \quad (12)$$

or

$$\Delta G_f^0 = 338,760 - 993.6T \text{ (J mol}^{-1}\text{)} \quad (13)$$

using Turkdogan (2000) or Jung and Hudon (2012), respectively.

### 2.3.2. The $P_2O_5$ activity coefficient $\gamma_{P_2O_5}$

As discussed in section 2.3.1, an estimate of the activity coefficients of the metal oxides in the non-ideal molten silicate, relative to the pure liquid oxides, is required in MAGMA. MAGMA normally uses an empirical model to calculate the metal oxide activity coefficients as a function of temperature and concentration (Fegley and Cameron, 1987), based on the formation of complex oxide and silicate pseudo-components that are assumed to mix ideally in the melt. Thus, pure liquid  $P_2O_5$  may combine with other liquid oxides present in the silicate melt to form orthophosphates of the general type  $M_3(PO_4)_2$ , where M represents varying amounts of the major metals such as Ca, Mg, Fe, Mn or Na (Buchwald, 1984). Phosphorus in the terrestrial crust occurs primarily in F-rich apatite solid solution, whereas phosphate minerals such as whitlockite –  $Ca_9(Mg, Fe)Na(PO_4)_7$  – are less abundant (Lodders and Fegley, 2011). In meteorites and lunar rocks, several types of terrestrial phosphates have been identified, such as whitlockite, chlorapatite –  $Ca_5(PO_4)_3Cl$ , hydroxyapatite –  $Ca_5(PO_4)_3OH$ , sarcopside –  $(Fe, Mn)_3(PO_4)_2$ , and graf-tonite –  $Ca_9(Mg, Fe)Na(PO_4)_7$  (Buchwald, 1984). Certain other phosphates are particular to extraterrestrial rocks, such as briarite –  $Na_2CaMg(PO_4)_2$  and panethite –  $Na_2(Mg, Fe)(PO_4)_2$  (Buchwald, 1984). In fact, orthophosphates are not well defined in meteorite samples due to their low occurrence and the difficulty in identifying the main phosphorus-bearing minerals in small grains. Nevertheless, the presence of whitlockite has been reported by Fuchs (1962) in several chondritic samples by using X-ray diffraction measurements, and Rojkovic et al. (1997) in the Rumanova H5 chondrite. Furthermore, Ward et al. (2017) systematically analysed various asteroidal bodies, including 1 carbonaceous chondrite and 8 ordinary chondrites, and reported that

Ca-phosphates are primarily found as apatite-group minerals and mer-rillite – an anhydrous member of the whitlockite group (Adcock et al., 2017).

In the present study, to calculate the activity coefficient of  $P_2O_5$  in MAGMA, the concentration of CaO,  $Al_2O_3$ , and  $P_2O_5$  in the silicate melt are reduced by the following reactions:



The corresponding thermodynamic data of  $\beta$ - $Ca_3(PO_4)_2$  whitlockite and  $AlPO_4$  berlinite in the solid phase are taken from Robie et al. (1979). In CABMOD, the thermodynamic properties of the solid phases of whitlockite and berlinite have to be extrapolated to temperatures above 3000 K from data below 1600 K, because of the lack of available thermodynamic data for the liquid phases of whitlockite and berlinite. Several points need to be noted: 1) up to 7 wt% of MgO, FeO, and  $Na_2O$  may appear in whitlockite inclusions, but there is a lack of information about the effects of these components on the stability of whitlockite (Zhai et al., 2014); 2) we have included the thermodynamics of berlinite in the present study as a potential pseudo-component that might form in the non-ideal silicate melt, even though the presence of this mineral in meteorite samples does not appear to have been reported; and 3) the present study does not include the thermodynamics of apatite due to the absence of available data. Table 2 shows the thermodynamic data for the activities of phosphorus pseudo-species.

In the present study we have compared the Ideal Mixing model of the complex components discussed above to calculate the activity coefficients of  $P_2O_5$ ,  $\gamma_{P_2O_5}$ , with a Regular Solution model (Ban-Ya, 1993) and two independent empirical formalisms based on a review of existing thermodynamic data (Suito et al., 1981; Turkdogan, 2000). These approaches have been used to describe the phosphorus distribution between molten steel and multicomponent slag, and have been widely investigated and applied in the glassmaking and metallurgical industries. Phosphorus is one of the main impurities in molten steel, and hence it is critical to control the P content in order to get a high quality steel (Li et al., 2019; Yang et al., 2018; Khadhraoui et al., 2019). The basic CaO–SiO<sub>2</sub>–MgO–FeO– $P_2O_5$  system present during the steelmaking process may therefore be extrapolated to a chondritic composition. Additionally, these empirical models provide an approximate evaluation of the activity coefficients of the hypothetical molten pure  $P_2O_5$  regardless of the mineral form of the phosphorus source. Furthermore, the content of  $P_2O_5$  in the experimental slags used in the assessment of  $\gamma_{P_2O_5}$  is normally <3 wt% (Turkdogan and Pearson, 1953; Suito et al., 1981; Suito and Inoue, 1982; Ban-Ya et al., 1991), consistent with the CI-chondrite composition of 0.34 wt%  $P_2O_5$  (Table S1 in the Supporting Information). As mentioned above, we investigated three approaches: first, Suito et al. (1981) used the original estimate of  $\Delta G_f^0$  for  $P_2O_5$  (Turkdogan and Pearson, 1953) and assessed experimentally the temperature dependence of  $\gamma_{P_2O_5}$  in MgO-saturated slags of the system CaO–MgO–FeO–SiO<sub>2</sub>; second, Ban-Ya (1993) developed a model for a liquid silicate melt to describe the slag-metal reactions and the distribution of phosphorus in the steelmaking process using a quadratic formalism based on a Regular Solution model; and, finally, Turkdogan (2000) revised his previous estimate of  $\Delta G_f^0(P_2O_5)$  and concluded that  $\gamma_{P_2O_5}$  depends ultimately on the content of  $P_2O_5$  and CaO. A detailed description of the three approaches can be found in the Supporting Information.

## 3. Results and discussion

### 3.1. Oxidation state of phosphorus in cosmic dust samples

The P K edge peaks in XANES spectra contain information on the oxidation state and coordination environment of P rich regions of the

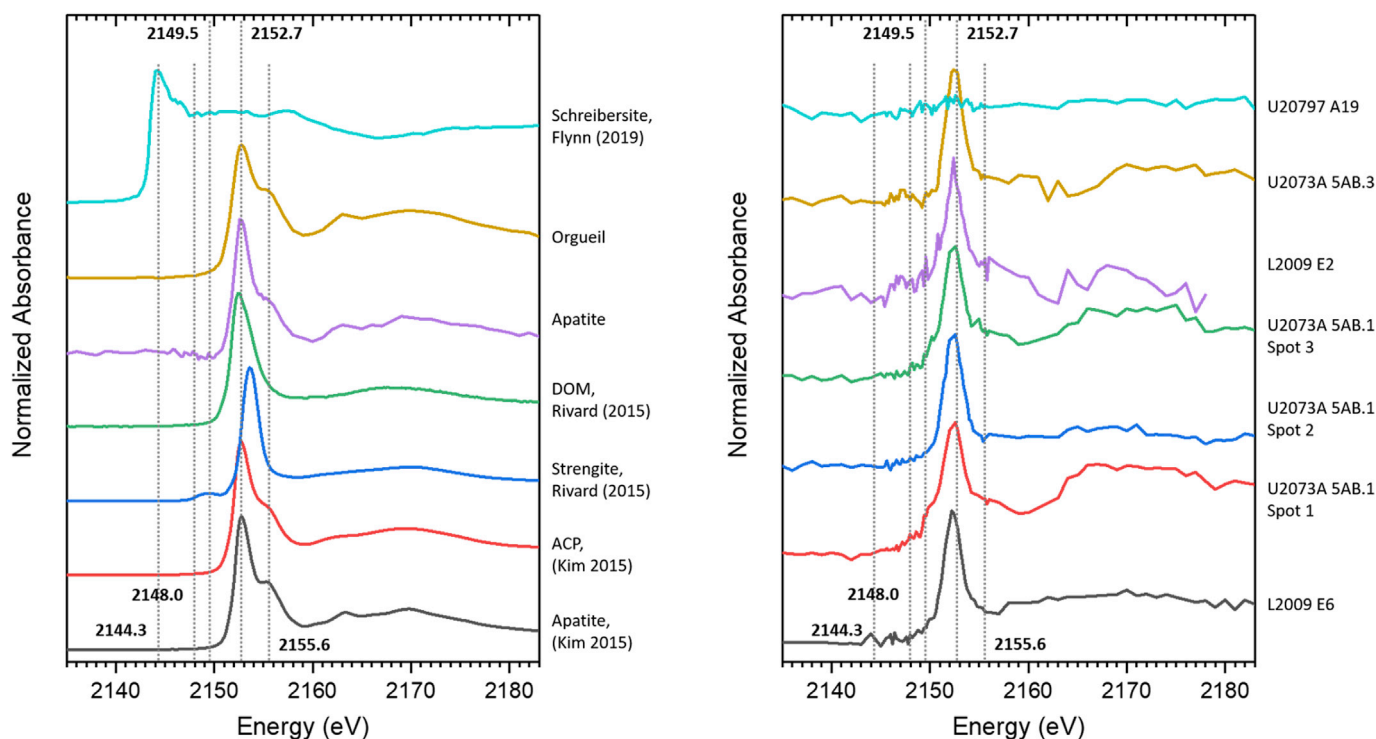


**Fig. 2.** Extracted P-XANES spectra from selected phosphorus hotspots present in the IDP, Apatite, and Orgueil samples, together with an Apatite and amorphous calcium phosphate (ACP) reference spectrum (Kim et al., 2015a), a Strengite and dissolved organic matter (DOM) reference spectrum (Rivard et al., 2016), and a Schreibersite reference spectrum (Flynn et al., 2019a). The dotted lines in the figure illustrate the approximate positions of: the white line for P as phosphide in the mineral Schreibersite (oxidation state  $-1$ ) at 2144.3 eV; the white line for P as phosphite (oxidation state  $+3$ ) at 2148 eV; a pre edge feature relating to Fe(III) phosphate minerals such as Strengite at 2149.5 eV; the white line of P as phosphate in the mineral Apatite (oxidation state  $+5$ ) at 2152.7 eV; and a post edge feature relating to crystalline calcium phosphate as in the mineral Apatite at 2155.6 eV. Note that the spectra are offset vertically for clarity.

sample slices. A change in the chemical environment is generally clearly discernible in the XANES spectra. The most notable change in the spectra lies in the position of the white line, which shifts to higher energies as the oxidation state of the phosphorus increases: moving from red phosphorus through phosphite to phosphate (i.e. oxidation states 0,  $+3$ , to  $+5$ ) the white line shifts from approximately 2144 eV to 2148 eV and 2152 eV, respectively (Küper et al., 1992; Küper and Hormes, 1994). The oxidation state of phosphorus in inorganic phosphides, such as the iron/nickel mineral schreibersite, while intuitively  $-3$  is in fact closer to  $-1$  (Grosvenor et al., 2005; Bryant et al., 2013; Pirim et al., 2014), and as such exhibits a white line close to that seen for P(0) in red phosphorus. Changes in the coordination environment of the phosphorus may also result in shifts of the white line position; however, these changes are typically small for different samples in which the oxidation state of the phosphorus is the same, making identification of the sample by the white line position alone difficult. Instead, differentiation usually lies in the pre- and post-edge features visible in the XANES spectra (Brandes et al., 2007; Ingall et al., 2011; Li et al., 2015).

Fig. 2 shows a selection of P-XANES spectra for various phosphorus hotspots found in the sample slices, together with literature spectra of crystalline (apatite) and amorphous calcium phosphate (ACP) (Kim et al., 2015b), iron phosphate (strengite) (Rivard et al., 2016), and iron/nickel phosphide (schreibersite) (Flynn et al., 2019a,b). As can be seen, the XANES from the apatite and Orgueil samples match very well with the apatite reference spectrum, with the peaks of all three post edge features at 2156, 2163, and 2170 eV all clearly visible, suggesting the majority of calcium phosphate in these samples is in a crystalline, rather than amorphous, form. Looking at the spectra from the IDP samples, it is clear that phosphate is the dominant form of P in these IDPs, with no evidence of any schreibersite or other reduce forms of P. It should be noted that XANES spectra extracted from the other P hotspots identified in the IDP samples were consistent with those shown in Fig. 2, albeit with slightly

poorer signal-to-noise ratios. Several studies have been performed on the phosphorus *K*-edge XANES spectroscopy of a range of apatite group minerals (Brandes et al., 2007; Ingall et al., 2011; Li et al., 2015). These studies indicated that apatite group minerals, that is calcium phosphate type minerals, could be identified by a distinct shoulder or widening on the main absorption peak centered around 2155.6 eV. Such a feature can be discerned in the spectra of samples L2009 E2, U2073A-5AB1 spot 3, and U2073A-5AB1 spot 1. This feature is not as clear as the feature in the apatite or ACP spectra, suggesting a mixed metal calcium phosphate mineral (e.g. Ca-Fe or Ca-Mg phosphate minerals). The absence of this feature in the other spectra (U2073A-5AB3, U2073A-5AB1 spot 2, and L2009E6), indicates that there are at least two distinctly different P bearing minerals in these IDPs. Identification of these minerals is difficult. No clear pre-edge feature at 2149.5 eV, an indication of an Fe(III) phosphate mineral such as strengite, is observed in these spectra; however, such a feature could easily be below the signal-to-noise ratio of the collected spectra.

A closer inspection of the white line peak positions in the IDP samples indicates that they are slightly lower in energy, by around 0.3–0.4 eV, when compared to the white line peak position of the apatite standard (Table 1). Although these shifts in peak position are small, they are larger than any expected drift in the X-ray beam energy, which is stable to within 0.1 eV for a given experimental setup. One possible explanation for this shift to lower energies is the presence of organic bound phosphate in these P hotspots. Rivard et al. (2016) and Giguet-Covex et al. (2013) have shown that organic phosphates can have white line peak positions ranging from 2152.4 to 2152.8 eV, typically with broad post-edge resonances (see the DOM spectrum Fig. 2). Although many of the XANES spectra of the IDP samples appear to have sharper post-edge features than would be expected for an organic phosphate sample, the small shift in the position of the white line, and the often poor signal to noise of the spectra, mean we cannot rule out the presence of organic phosphates in our samples.

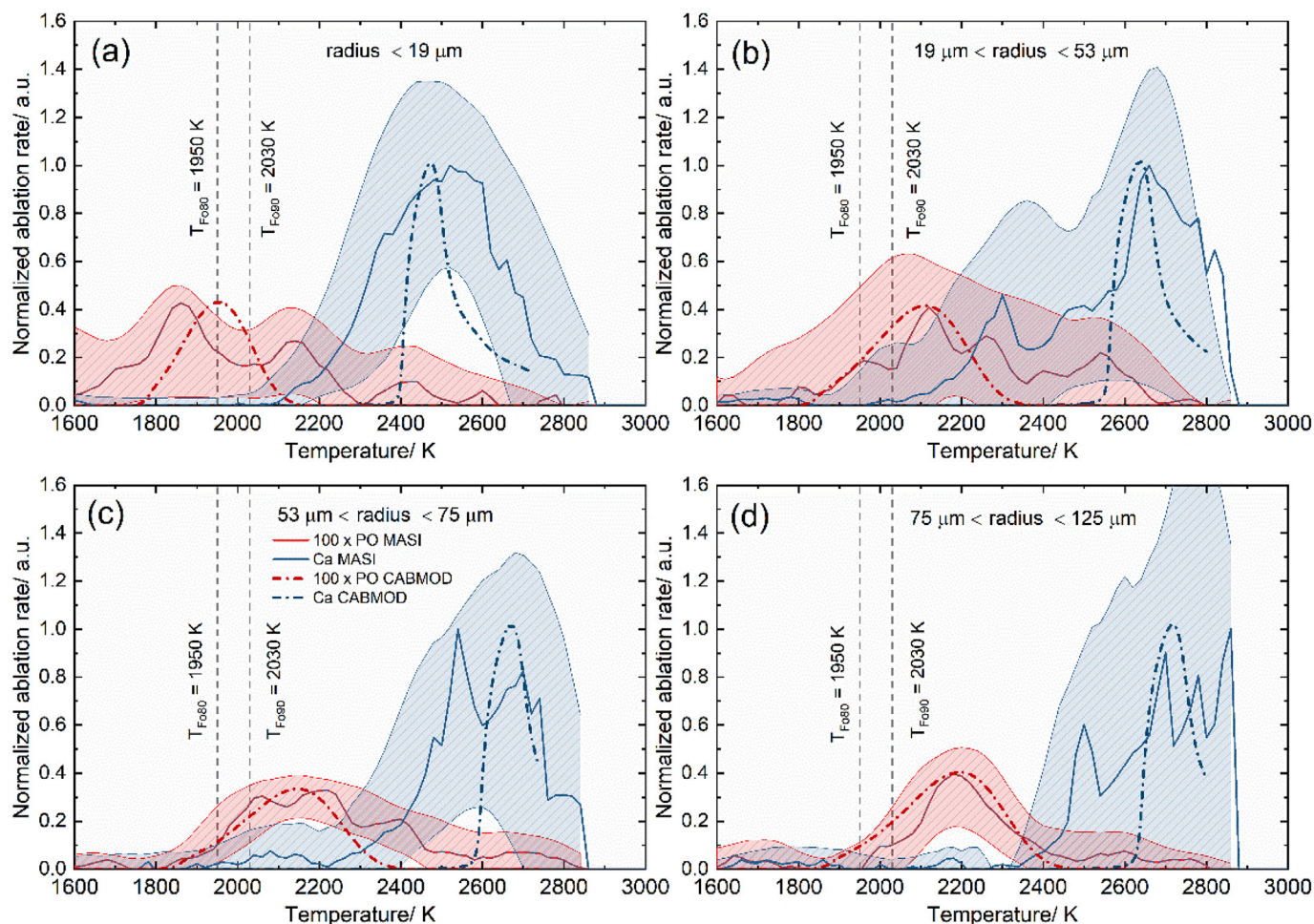


**Fig. 3.** Normalized PO and Ca LIF profiles measured by MASI and resulting from linear temperature ramps ( $T = c_1 + c_2t$ ) applied to Allende meteorite particles for 4 different average radii, (a) 9.5  $\mu\text{m}$ , (b) 36  $\mu\text{m}$ , (c) 64  $\mu\text{m}$ , and (d) 100  $\mu\text{m}$ . Solid red and blue lines represent the averaged PO and Ca signals, respectively. Thick dash-dot red and blue lines correspond to CABMOD prediction assuming the model of [Turkdogan \(2000\)](#) for the Gibbs free energy of  $\text{P}_2\text{O}_5$  ( $\Delta G_f^\circ$ ) and the Regular Solution ([Ban-Ya, 1993](#)) for  $\gamma_{\text{P}_2\text{O}_5}$ . The red and blue shaded regions represent experimental uncertainty envelopes for PO and Ca, respectively. The vertical dashed-lines represent the melting temperature of  $\text{Fo}_{80}$  ( $T = 1950$  K) and  $\text{Fo}_{90}$  ( $T = 2030$  K). (For interpretation of the references to colour in this figure legend, the reader is referred to the Web version of this article.)

The absence of any reduced forms of P in our XANES spectra can be interpreted in several ways. One interpretation is that the CP-IDPs entering the Earth's atmosphere contain little or no reduced forms of phosphorus, with the majority of P in the form of phosphate. Another interpretation is that these CP-IDPs may have contained reduced forms of P, which have become oxidized during infall or collection, while a third interpretation is that our analysis is primarily looking at the surface mineralogy, rather than at the bulk material. Indeed [Pirim et al. \(2014\)](#) have shown that the surfaces of meteorite schreibersite inclusions and schreibersite surrogates can be oxidized at low temperatures ( $\sim 298$  K) by reaction with  $\text{O}_2$ , to produce iron phosphate. However, the oxidized layer is only around 10 nm thick, with the deeper mineralogy remaining unchanged. As our IDP slices are significantly thicker (70–100 nm thick), we are very unlikely to be looking only at an oxidized surface, especially as many of the P hotspots we observed in our samples were typically hundreds of nm across, and are from central slices of the IDPs.

Bulk oxidation of any reduced phosphorus could occur if the IDPs were heated to temperatures at which they become molten and oxygen was able to diffuse throughout the particles. As discussed in this paper and evidenced by cosmic spherules collected at the Earth's surface, many IDPs entering the Earth's atmosphere do heat up to temperatures ( $\sim 1800$  K) at which they melt ([Vondrak et al., 2008](#)). However, the IDPs collected for analysis in this study exhibit no evidence of melting, most

probably because they are relatively small and would have entered the atmosphere at relatively low velocities, so that excess heat was effectively radiated away ([Grün et al., 2019](#)). Indeed, the images of IDPs collected by NASA show them to be fractal-like (fluffy) materials, very unlike melted micrometeorites and cosmic spherules collected at the Earth's surface ([Maurette et al., 1991](#)). Additional evidence indicating that the collected IDPs do not become molten is the presence of un-oxidized sulphides. The bulk oxidation of both phosphides and sulphides would require the particles to become molten, to allow diffusion of oxygen throughout the particles. However, S-XANES on 2 large, cluster IDPs indicates the presence of Fe-sulphides, with few of the particles studied showing signs of significant sulphur oxidation ([Flynn et al., 2015](#)). The presence of sulphides in IDPs suggest that if phosphides were the dominant form of P in IDPs, then at least some phosphide would remain un-oxidized after atmospheric entry. As we see no evidence of any phosphide, or even other reduced forms of P (oxidation state  $\leq +3$ ), this suggests that the oxidized P we observe is not the result of P being oxidized during infall and collection, but is rather the form of P in CP-IDPs before they enter the Earth's atmosphere. Nevertheless, we note that to state this unequivocally a larger collection of IDPs would need to be analysed, and further work conducted on the temperature at which reduced forms of P (oxidation state  $\leq +3$ ) are oxidized in a 20% oxygen atmosphere.

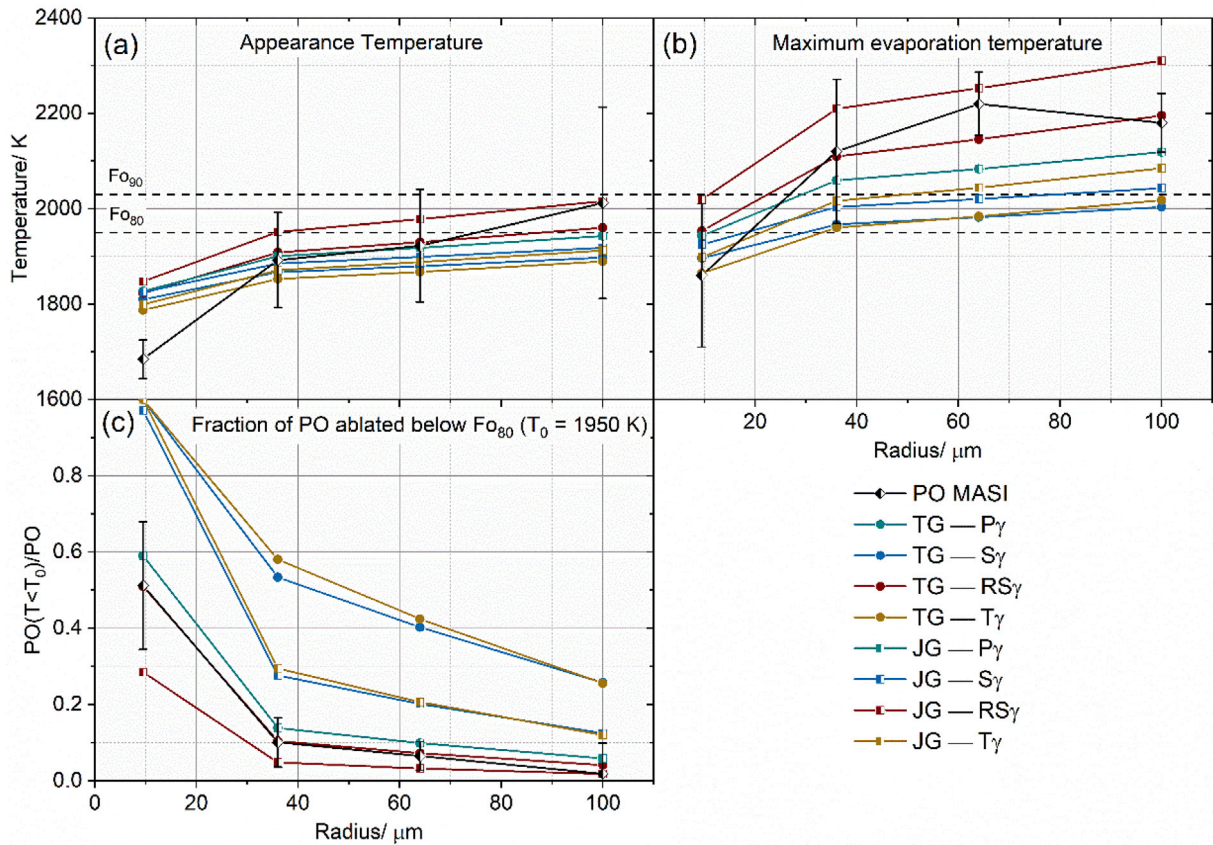


Fig. 4. Appearance temperature (a) that corresponds to 5% of PO ablated, temperature at the maximum evaporation (b), and fraction of PO ablated below  $Fo_{80}$  ( $T = 1950$  K) for Allende samples (c). The horizontal dashed-lines represent the melting temperature of  $Fo_{80}$  ( $T = 1950$  K) and  $Fo_{90}$  ( $T = 2030$  K). Black dots correspond to MASI measurements. Green, blue, red, and orange dots and squares show the CABMOD prediction for each of the models for the Gibbs free energy of  $P_2O_5$  ( $\Delta G_f^0$ ) and  $\gamma_{P_2O_5}$  discussed in the main text. TG and JG correspond to the models of Turkdogan (2000) and Jung and Hudon (2012) for  $\Delta G_f^0$ , whereas  $P\gamma$ ,  $S\gamma$ ,  $RS\gamma$ , and  $T\gamma$  correspond to the models of Pseudo-components (Fegley and Cameron, 1987), Suito et al. (1981), Regular Solution (Ban-Ya, 1993), and Turkdogan (2000) for  $\gamma_{P_2O_5}$ .

In summary, our results strongly indicate that phosphate is the dominant form of phosphorus in CP-IDPs. With dust particles accounting for around 99% of the total annual mass influx of exogenous material to the atmospheres of the terrestrial planets (Plane et al., 2017), and with the bulk of IDPs entering these atmospheres being chondritic in nature, then phosphate should be the major form of phosphorus entering these atmospheres. Although a significant portion of these dust particles will ablate on entry, the majority (~70%) will survive as unmelted micrometeorites and cosmic spherules (Carrillo-Sánchez et al., 2020), delivering phosphate to the surfaces of these planets. Although from the XANES spectra we have not been able to identify the exact phosphate minerals present in the IDPs, our results indicate that the samples contain at least two distinct phosphate bearing groups. One is an apatite group mineral, and the other could be organic phosphates or other mineral forms of phosphate.

### 3.2. Comparison of MASI results with CABMOD

In this section, we present a comparison between the MASI ablation profiles and CABMOD modelling results for the Allende and apatite samples. Calcium phosphate minerals thus far detected in Allende, a CV3 carbonaceous chondrite, are apatite, whitlockite and merrillite (Wlotzka, 1976; Armstrong et al., 1985; Ebihara and Honda, 1987; Rubin, 1991) along with other phosphates such as panethite ( $Na(Fe,Mg)PO_4$ ) and small amounts of phosphide (e.g. schreibersite (Campbell et al., 2003)). Eight different thermodynamic models of phosphorus were tested within MAGMA. These were constructed by choosing for

$\Delta G^0(P_2O_5(l) = 2P(g) + 5O(g))$  either the estimate from Turkdogan (2000) (equation [12], hereafter TG) or from Jung and Hudon (2012) (equation [13], hereafter JG), in combination with one of the four different estimates for the activity coefficient  $\gamma_{P_2O_5}$  (see Section 2.3.2): that is, formation of pseudo-components in the non-ideal silicate melt (equations [14] and [15], hereafter  $P\gamma$ ), Suito et al. (1981) (equation [16], hereafter  $S\gamma$ ), the Regular Solution provided by Ban-Ya (1993) (equations [17] and [18], hereafter  $RS\gamma$ ), and Turkdogan (2000) (equation [20], hereafter  $T\gamma$ ).

#### 3.2.1. Allende samples

Fig. 3 illustrates the (normalized) LIF signals from PO and Ca as a function of temperature, for four different sample sizes. The panels in Fig. 4 show the appearance temperature of PO, the temperature of its ablation rate peak, and the fraction of PO ablated below the melting point of  $Fo_{80}$  olivine ( $T < 1950$  K), predicted by CABMOD for the eight P thermodynamic models. The combinations TG- $RS\gamma$  and JG- $RS\gamma$  best reproduce the appearance temperature of the PO ablation signal (5% of PO ablated) measured by MASI for particle radii  $> 19$  μm, whereas other combinations (TG- $P\gamma$ , TG- $S\gamma$ , TG- $T\gamma$ , JG- $P\gamma$ , JG- $S\gamma$ , and JG- $T\gamma$ ) predict somewhat lower appearance temperatures (although the 8 models are within the uncertainty range). Note that all models fail to reproduce the appearance temperature of the MASI PO ablation signal for the particle radius  $< 19$  μm, indicating that the representative average size of the first size bin is surely smaller than the average radius of 9.5 μm. Fig. 4b indicates that TG- $RS\gamma$  (in particular) and JG- $RS\gamma$  also capture satisfactorily the temperature of the maximum PO ablation rate for the Allende samples. In contrast, the other combinations predict that phosphorus is

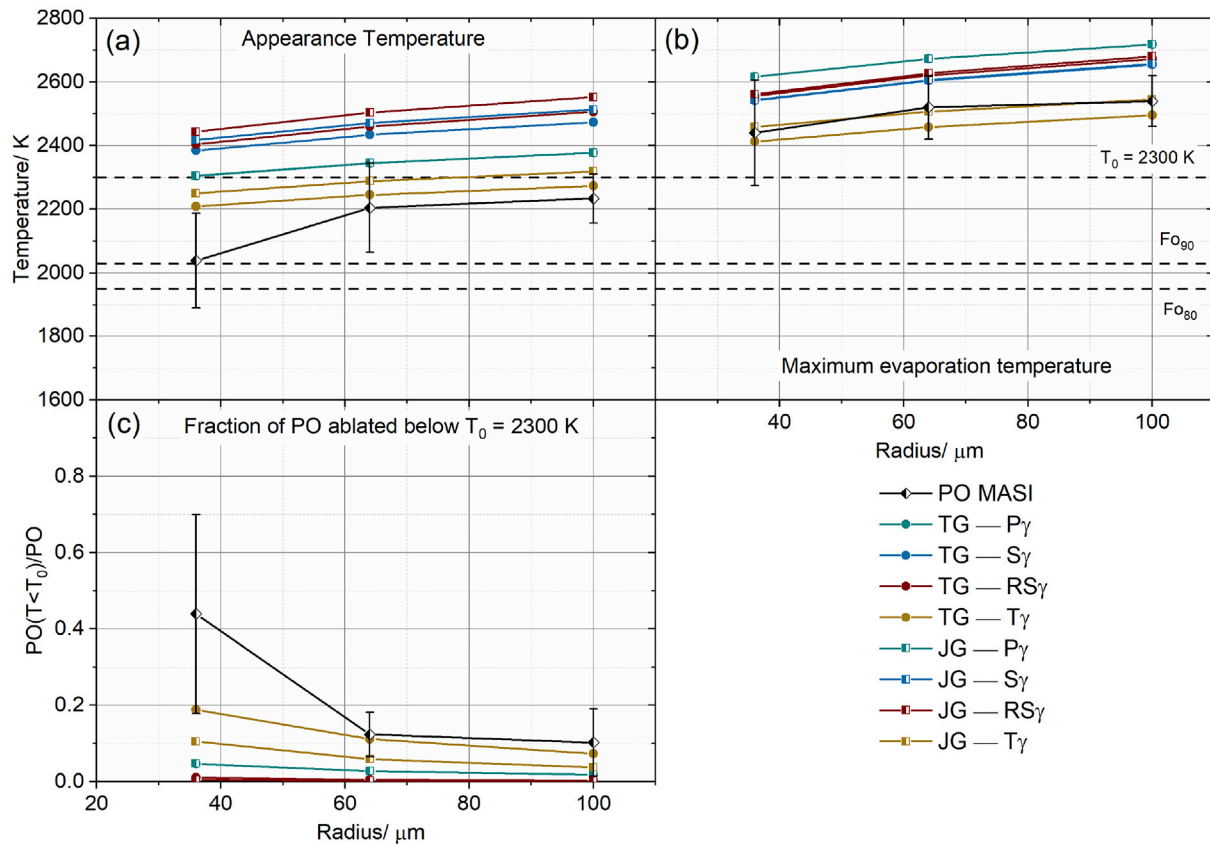


Fig. 5. Appearance temperature (a) that corresponds to 5% of PO ablated, temperature at the maximum evaporation (b), and fraction of PO ablated below  $F_{O_{80}}$  ( $T = 1950$  K) for Apatite samples (c). The horizontal dashed-lines represent the melting temperature of  $F_{O_{80}}$  ( $T = 1950$  K),  $F_{O_{90}}$  ( $T = 2030$  K), and the threshold temperature  $T_0 = 2300$  K. Black dots correspond to MASI measurements. Green, blue, red, and orange dots and squares show the CABMOD prediction for each of the models for the Gibbs free energy of  $P_2O_5$  ( $\Delta G_f^\theta$ ) and  $\gamma_{P_2O_5}$  discussed in the main text. In the plot, TG and JG correspond to the models of Turkdogan (2000) and Jung and Hudon (2012) for  $\Delta G_f^\theta$ , whereas  $P_\gamma$ ,  $S_\gamma$ ,  $RS_\gamma$ , and  $T_\gamma$  correspond to the models of Pseudo-components (Fegley and Cameron, 1987), Suito et al. (1981), Regular Solution (Ban-Ya, 1993), and Turkdogan (2000) for  $\gamma_{P_2O_5}$ .

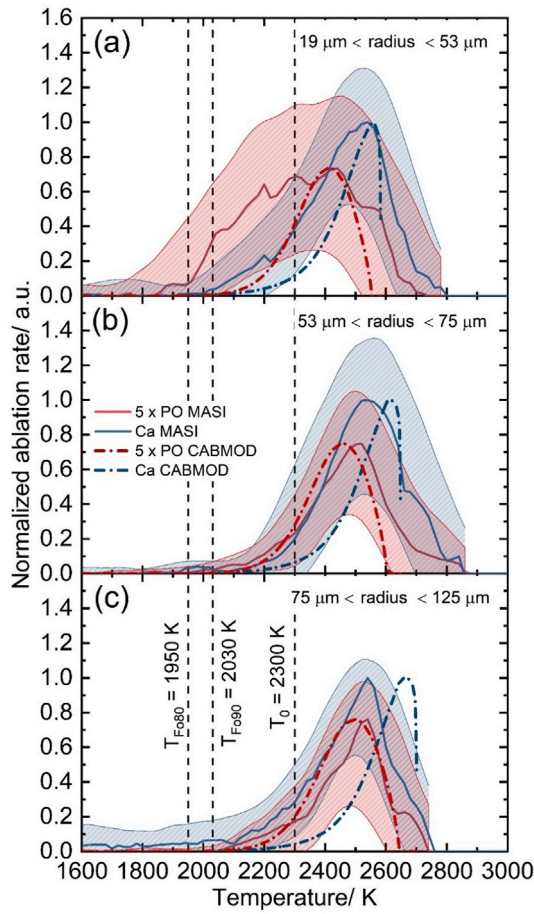
markedly more volatile, with temperatures around 100 K below the experimental values for radius  $>19$   $\mu\text{m}$ , and with ablation peaks between the melting temperature of  $F_{O_{80}}$  and  $F_{O_{90}}$ . Finally, Fig. 4c indicates that once more TG- $RS_\gamma$  and JG- $RS_\gamma$  produce the best agreement for the fraction of PO ablated below the melting point of  $F_{O_{80}}$ , whereas the other models over-emphasize the volatility of PO. Consequently, TG- $RS_\gamma$  produces the overall best agreement with the MASI experiments, and therefore this model combination was adopted as the reference for determining the atmospheric ablation profiles of phosphorus in Section 3.4.

Fig. 3 compares the CABMOD predictions for evaporation of PO and Ca from Allende using TG- $RS_\gamma$ , with MASI for different particle sizes. In all cases, PO ablates before Ca. CABMOD provides reliable evaporation rates for PO, reproducing the onset and the ablation peak of the experimental pulses for radius  $>19$   $\mu\text{m}$ . Fig. S1 in the Supporting Information shows that JG- $RS_\gamma$  simulates the breadth of experimental PO pulses better than TG- $RS_\gamma$ , even though the temperature ablation peaks are shifted  $\sim 100$  K to higher temperatures. A caveat is that the experimental profiles are significantly broader at high temperatures ( $T > 2400$  K) due to the combination of several effects (Gómez-Martín et al., 2017): 1. Liquid electromigration of the molten particles along the tungsten filament in the MASI, which significantly affects the evaporation of more refractory elements; 2. Molten particles lose surface area because of the filling of pores and cavities, thus reducing the evaporation efficiency compared with CABMOD; and 3. Each experimental ablation profile determined by MASI is the average of several particles with a range of sizes within the limits of the bin size. Fig. 3 also shows that the

temperature of the ablation peak of PO is located between 2100 K and 2200 K for radius  $>19$   $\mu\text{m}$ . Fig. S3 in the Supporting Information shows the profiles of individual experiments used to estimate this averaged PO profile.

### 3.2.2. Apatite samples

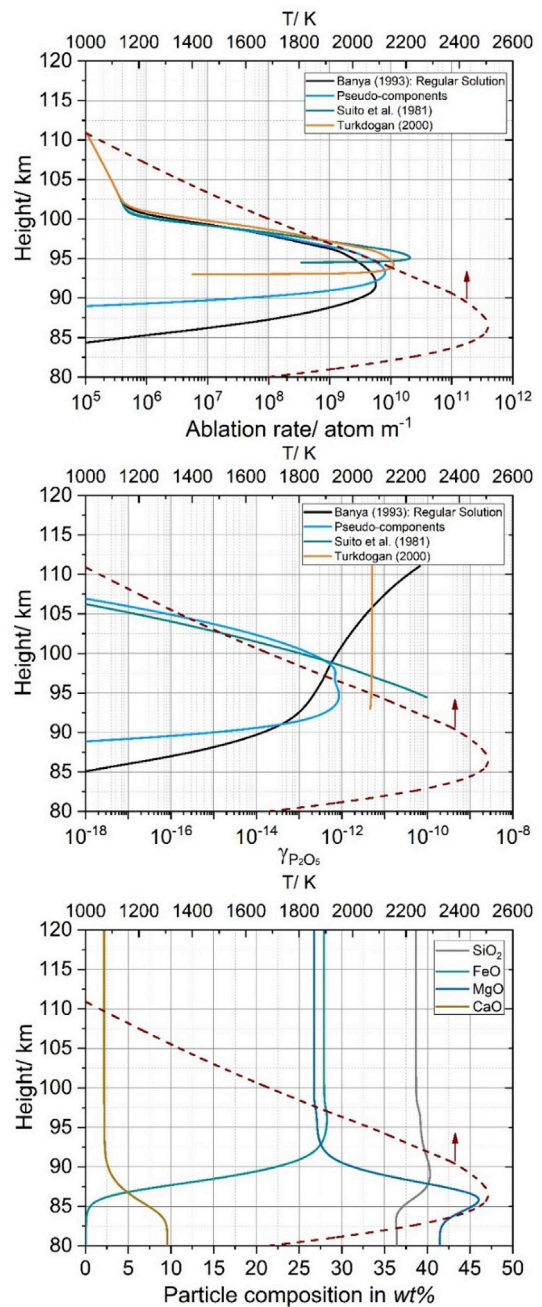
In order to test the PO ablation signal measured by MASI, some experiments with apatite samples were carried out, again using linear temperature ramps. The content of  $P_2O_5$  in the apatite samples is high, 43.1 wt% (see Table S1), and so this is useful for assessing the detectability of the PO signal by LIF in the MASI. However, as discussed in Section 2.3.2, most of the models based on steelmaking slags are only valid for low- $P_2O_5$  slags, albeit Turkdogan (2000) proposed a solution for slags containing 10 to 40 wt%  $P_2O_5$  (equation [S6] in the Supporting Information). In the present study, to be consistent with the valid range given by Turkdogan (2000), the contents of  $P_2O_5$  and CaO are set to 40 wt% and 60 wt%, respectively. Fig. 5a shows that TG- $T_\gamma$  reproduces better the appearance temperature for the two larger sizes. Fig. 5b shows that both the TG- $T_\gamma$  and JG- $T_\gamma$  combinations in CABMOD provide reliable estimates for the temperature of the ablation peak, except for the smaller size, whereas Fig. 5c shows that TG- $T_\gamma$  is the only model that can reproduce the fraction of PO ablated below 2300 K (note that this temperature is arbitrarily selected between the melting point of  $F_{O_{90}}$ , 2030 K, and the melting point of CaO, 2845 K). Fig. 6 shows differential ablation between PO and Ca for sizes below 53  $\mu\text{m}$ , whereas they follow a similar evaporation pattern for larger radii. Fig. S4 in the Supporting Information shows the profiles from individual experiments used to estimate the averaged PO profile.



**Fig. 6.** Normalized PO and Ca LIF profiles measured by MASI and resulting from linear temperature ramps ( $T = c_1 + c_2t$ ) applied to Apatite samples for 3 different average radii, (a) 36  $\mu\text{m}$ , (b) 64  $\mu\text{m}$ , and (c) 100  $\mu\text{m}$ . Solid red and blue lines represent the averaged PO and Ca signals, respectively. Thick dash-dot red and blue lines correspond to CABMOD prediction assuming the model of Turkdogan (2000) for the Gibbs free energy of  $\text{P}_2\text{O}_5$  ( $\Delta G_f^\circ$ ) and for  $\gamma_{\text{P}_2\text{O}_5}$ . The red and blue shaded regions represent experimental uncertainty envelopes for PO and Ca, respectively. The vertical dashed-lines represent the melting temperature of  $\text{Fe}_{90}$  ( $T = 1950$  K),  $\text{Fe}_{90}$  ( $T = 2030$  K), and the threshold temperature  $T_0 = 2300$  K. (For interpretation of the references to colour in this figure legend, the reader is referred to the Web version of this article.)

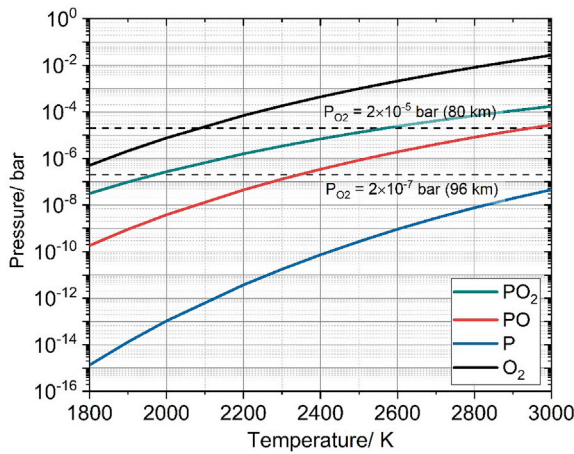
### 3.3. Ablation of phosphorus – CABMOD simulations

Fig. 7a shows the ablation rates of phosphorus predicted by CABMOD from a 1  $\mu\text{g}$  meteoroid entering at 20  $\text{km s}^{-1}$  and calculated by the four thermodynamic models discussed above. In terms of volatility of phosphorus, the models of Suito et al. (1981) and Turkdogan (2000) produce higher ablation peaks than those based on the formation of pseudo-species in the molten silicate bulk or the Regular Solution (Ban-Ya, 1993). In addition, Fig. 7a shows that the profile predicted by the Regular Solution is markedly broader spanning around 15 km, whereas high-volatility models predict narrower profiles, as shown by the model based on Suito et al. (1981). Fig. 7b and c illustrate the vertical profiles of the activity coefficients determined by the different models and the compositional evolution of  $\text{SiO}_2$ , FeO, MgO, and CaO within the particle in %wt. The activity coefficients shown in Fig. 7b correspond to the altitude range at which the ablation of phosphorus occurs according to the different models. Fig. 7b shows that Suito et al. (1981) predicts that  $\gamma_{\text{P}_2\text{O}_5}$  increases with increasing temperature (see equation S1 in the Supporting Information), whereas the model of Turkdogan (2000) assumes that  $\gamma_{\text{P}_2\text{O}_5}$  is independent of temperature and it only depends on the content of CaO and



**Fig. 7.** (a) Ablation rates of phosphorus in the Earth’s upper atmosphere predicted by CABMOD from a 1  $\mu\text{g}$  meteoroid entering at 20  $\text{km s}^{-1}$  and calculated by the four thermodynamic models: Regular Solution in black (Ban-Ya, 1993), pseudo-components in blue (Fegley and Cameron, 1987), model of Suito et al. (1981) in green, and model of Turkdogan (2000) in orange. (b) vertical profiles of the activity coefficients. (c) Compositional evolution of  $\text{SiO}_2$ , FeO, MgO, and CaO within the particle in %wt. The red dashed line in each panel is the particle temperature, referred to the top abscissa as shown by the red arrow. (For interpretation of the references to colour in this figure legend, the reader is referred to the Web version of this article.)

MgO in the particle (equation S5 in the Supporting Information). In contrast, according to the Regular Solution (see equations S2 and S3 in the Supporting Information),  $\gamma_{\text{P}_2\text{O}_5}$  decreases with increasing temperature and the evaporation of FeO below 95 km altitude emphasizes the lower volatility of  $\text{P}_2\text{O}_5$ , leading to the broader ablation profile illustrated in Fig. 7a. Fig. 7c displays the compositional evolution of  $\text{SiO}_2$ , FeO, MgO, and CaO within the particle in %wt during the ablation process.



**Fig. 8.** Temperature dependence of the ratio vapour pressures of P, PO and PO<sub>2</sub> calculated by MAGMA, assuming a CI-chondrite composition and the Regular Solution (Ban-Ya, 1993). The horizontal dashed lines indicate the range of atmospheric pressures in the Earth’s atmosphere where most of the ablation of phosphorus occurs.

MAGMA predicts that the vaporization of liquid P<sub>2</sub>O<sub>5</sub> from the non-ideal silicate melt produces P(g), P<sub>2</sub>(g), PO(g), and PO<sub>2</sub>(g), which are in equilibrium with the melt (see Table 2 for thermodynamic data for formation of phosphorus gases included in the vaporization calculations). Fig. 8 shows the temperature dependence of P, PO, PO<sub>2</sub> and O<sub>2</sub> calculated by MAGMA, assuming a CI-chondrite composition and the Regular Solution (Ban-Ya, 1993). In agreement with Pasek (2015), P (and P<sub>2</sub>) are very minor gas-phase species in the presence of oxygen. The ratio of PO to PO<sub>2</sub> increases with T, but PO<sub>2</sub> is dominant over the entire temperature range up to 3000 K. Also shown in Fig. 8 is the range of O<sub>2</sub> in the Earth’s atmosphere between ~80 and 96 km i.e. the region where most of the phosphorus ablates (see Section 3.4). This shows the O<sub>2</sub> produced by

evaporation from the melt has a higher pressure than the surrounding O<sub>2</sub> atmospheric pressure even at 80 km for temperatures above 2100 K, and is higher than the pressure at 96 km at the start of ablation when T = 1850 K. This indicates that the atmospheric O<sub>2</sub> may slightly increase the PO<sub>2</sub>:PO ratio of the ablating phosphorus, but this effect will be limited. The fate of the ablated PO<sub>2</sub> is discussed in more detail in Section 3.5.

### 3.4. Determining the phosphorus mass influx at Earth, Mars and Venus

As discussed in Carrillo-Sánchez et al. (2016, 2020), CABMOD estimates the ablation rate profiles of individual elements from a dust particle with specified mass, entry velocity, and zenith angle. The model is then combined with an astronomical model of dust production and evolution in the solar system to estimate the total injection of a range of elements into a planetary atmosphere. For this purpose, Carrillo-Sánchez et al. (2016, 2020) used the Zodiacal Cloud Model (ZoDy) (Nesvorný et al., 2010, 2011) constrained by observations of infrared emission measured by the Planck satellite (Ade et al., 2014), that suggests an average break diameter  $D_{\text{break}} \sim 36 \mu\text{m}$  (Fixsen and Dwek, 2002). ZoDy predicts the mass and velocity distributions for dust from three sources: the Jupiter-Family Comets (JFCs), Asteroid belt (ASTs) and Halley-Type Comets (HTCs). The injection rate profiles of the main meteoritic metals in the atmospheres of Earth, Mars, and Venus were estimated using a Monte-Carlo method to sample the velocity and zenith angle distributions of each individual particle in the mass range between 10<sup>-3</sup> and 10<sup>3</sup> μg and for each of the three cosmic dust sources. The procedure is described in detail in Carrillo-Sánchez et al. (2020), where we also determined the global mass injection rates at Earth, Mars and Venus to be 27.9 ± 8.1 t d<sup>-1</sup> (tonnes per Earth day), 2.1 ± 1.2 t d<sup>-1</sup>, and 31.0 ± 17.7 t d<sup>-1</sup>, respectively.

In the present study we now use the new version of CABMOD (Section 3.2) to estimate the global input rate of phosphorus in the upper atmospheres of Earth, Mars and Venus. We assume in CABMOD the CI chondritic elemental abundance of P normalized to Si is 8.2 × 10<sup>-3</sup> (Lodders and Fegley, 2011), which is close to the corresponding P abundance of

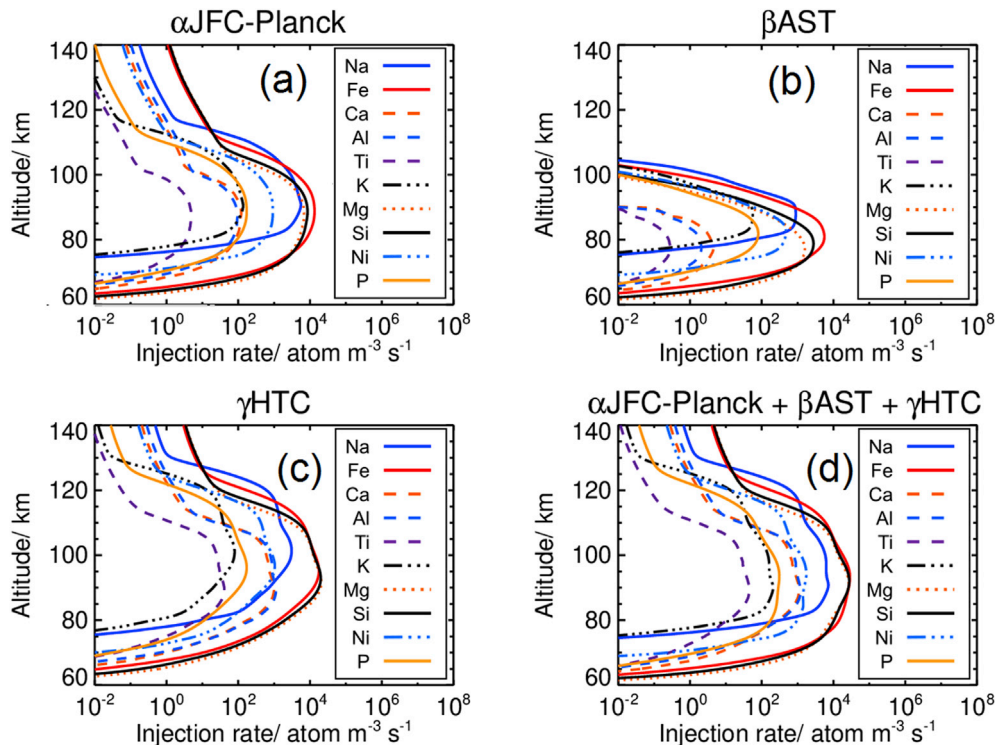


**Fig. 9.** (a), (b) and (c): Ablation rate profiles in the upper atmosphere of Earth for the main metal constituents and P, from the JFC (constrained with the Planck observations), AST, and HTC cosmic dust sources, respectively. (d): total ablation rates.

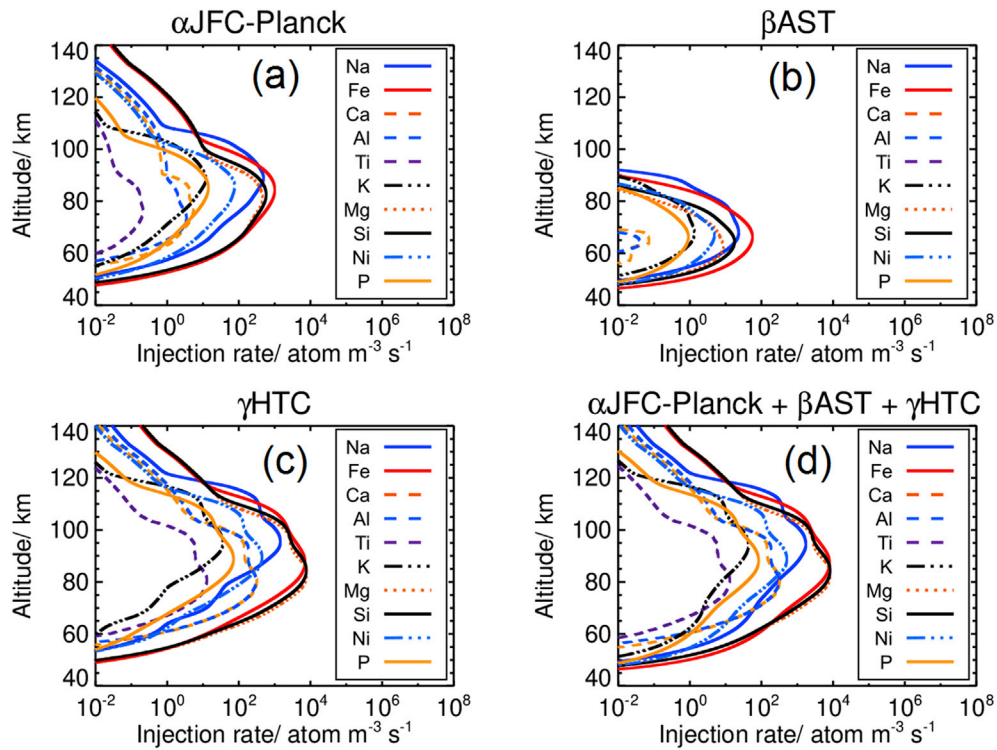


Fig. 10. (a), (b) and (c): Ablation rate profiles in the upper atmosphere of Mars for the main metal constituents and P, from the JFC (constrained with the Planck observations), AST, and HTC cosmic dust sources, respectively. (d): total ablation rates.

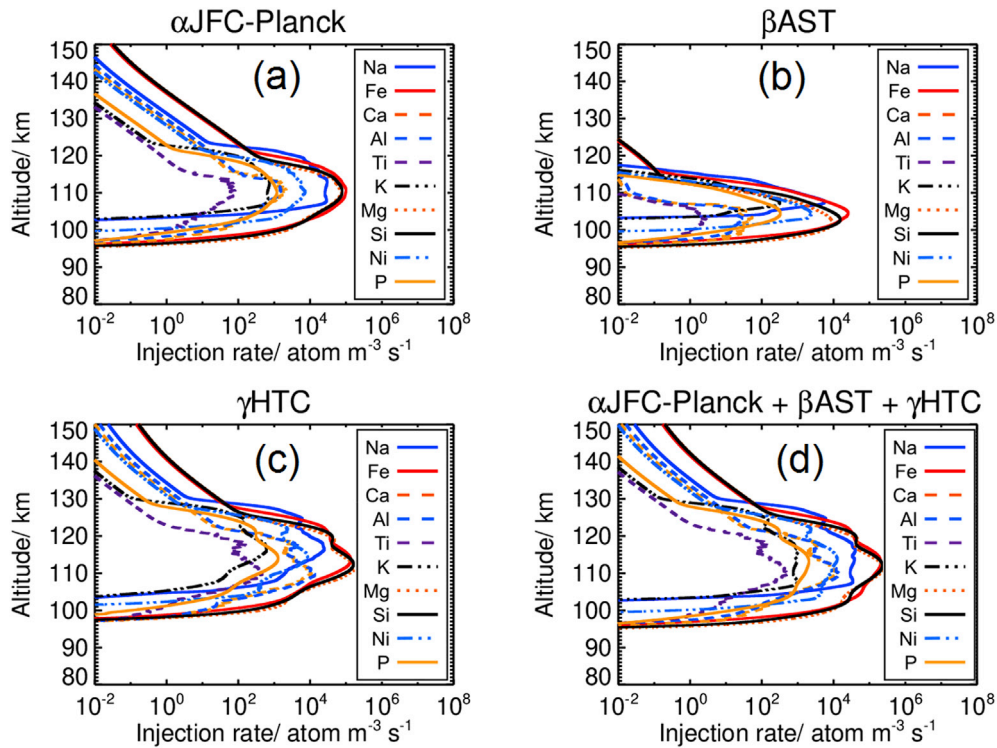


Fig. 11. (a), (b) and (c): Ablation rate profiles in the upper atmosphere of Venus (on the night-side) for the main metal constituents and P, from the JFC (constrained with the Planck observations), AST, and HTC cosmic dust sources, respectively. (d): total ablation rates.

Allende samples of  $5.7 \times 10^{-3}$  (Clarke et al., 1971). Figs. 9–11 show the injection rate profiles for individual metals and P injected into the upper atmospheres of Earth, Mars and Venus, respectively. Each figure shows the injection profiles from each of the three cosmic dust sources, and the

total ablation rates. In all cases, P exhibits an ablation profile similar to Ni and Fe, peaking well below the more volatile elements Na and K. Table 3 lists the global input rates as well as the ablation efficiencies of phosphorus for the three planets. The global P ablation rate is  $0.017 \text{ t d}^{-1}$

**Table 3**

Global mass input of phosphorus from the three cosmic dust sources (JFC-Planck, AST, and HTC) for Earth, Mars, and Venus. The partitioning of the phosphorus input between P, PO and PO<sub>2</sub>, and the total input are shown. The percentages in parentheses after the total inputs are the fraction of phosphorus that ablates from each dust source.

Mass influx	JFC (t d <sup>-1</sup> )	AST (t d <sup>-1</sup> )	HTC (t d <sup>-1</sup> )	Total P (t d <sup>-1</sup> )	Total ablated (t d <sup>-1</sup> )	Total influx (t d <sup>-1</sup> )
Earth	P	2.8 × 10 <sup>-5</sup>	1.6 × 10 <sup>-7</sup>	3.2 × 10 <sup>-5</sup>	6.1 × 10 <sup>-5</sup>	8.2 ± 8.1
	PO	1.1 × 10 <sup>-3</sup>	2.7 × 10 <sup>-4</sup>	1.2 × 10 <sup>-3</sup>	2.5 × 10 <sup>-3</sup>	
	PO <sub>2</sub>	6.0 × 10 <sup>-3</sup>	1.9 × 10 <sup>-3</sup>	6.8 × 10 <sup>-3</sup>	0.015	
	Total	7.1 × 10 <sup>-3</sup> (25%)	2.2 × 10 <sup>-3</sup> (57%)	8.0 × 10 <sup>-3</sup> (96%)	0.017 (41%)	
Mars	P	1.1 × 10 <sup>-6</sup>	6.0 × 10 <sup>-10</sup>	6.7 × 10 <sup>-6</sup>	7.8 × 10 <sup>-6</sup>	0.65 ± 1.2
	PO	1.8 × 10 <sup>-5</sup>	1.3 × 10 <sup>-6</sup>	1.3 × 10 <sup>-4</sup>	1.5 × 10 <sup>-4</sup>	
	PO <sub>2</sub>	1.5 × 10 <sup>-4</sup>	1.2 × 10 <sup>-5</sup>	8.2 × 10 <sup>-4</sup>	9.8 × 10 <sup>-4</sup>	
	Total	1.7 × 10 <sup>-4</sup> (11%)	1.3 × 10 <sup>-5</sup> (3%)	9.6 × 10 <sup>-4</sup> (93%)	1.2 × 10 <sup>-3</sup> (38%)	
Venus	P	3.4 × 10 <sup>-5</sup>	2.0 × 10 <sup>-7</sup>	5.4 × 10 <sup>-5</sup>	8.9 × 10 <sup>-5</sup>	12.7 ± 17.7
	PO	1.3 × 10 <sup>-3</sup>	2.5 × 10 <sup>-4</sup>	1.8 × 10 <sup>-3</sup>	3.3 × 10 <sup>-3</sup>	
	PO <sub>2</sub>	9.7 × 10 <sup>-3</sup>	1.6 × 10 <sup>-3</sup>	9.1 × 10 <sup>-3</sup>	0.020	
	Total	0.011 (36%)	1.9 × 10 <sup>-3</sup> (67%)	0.011 (98%)	0.024 (53%)	

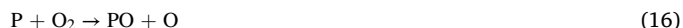
(Earth),  $1.15 \times 10^{-3} \text{ t d}^{-1}$  (Mars), and  $0.024 \text{ t d}^{-1}$  (Venus). The ablation efficiencies of P are 41% (Earth), 38% (Mars), and 53% (Venus), similar to the ablation yields of Ni and Fe (Carrillo-Sánchez et al., 2020). The CI chondritic P:Ca ratio is 0.14 (Lodders and Fegley, 2011), whereas the CABMOD-ZoDy simulation indicates the P:Ca ratio in the Earth's atmosphere should be 0.36, the nearly 3 times higher ratio reflecting the relative volatility of P compared to Ca.

### 3.5. Fate of ablated PO<sub>2</sub>

Table 3 shows that P is mainly released as PO<sub>2</sub> in the three planetary atmospheres with 85.0%, 85.9%, and 85.6% for Earth, Mars and Venus, respectively. PO makes up the next largest fraction (14.7%, 13.4%, and 14.0%, respectively), and P is less than 1%. Freshly ablated PO<sub>2</sub> molecules will initially have essentially the same velocity as the parent meteoroid. At the minimum velocity of  $12 \text{ km s}^{-1}$  for entry into the Earth's atmosphere, a PO<sub>2</sub> molecule will therefore have  $4.5 \text{ MJ mol}^{-1}$  of kinetic energy. The energy required to atomise PO<sub>2</sub> to P + 2O is  $1.1 \text{ MJ mol}^{-1}$  (calculated at the complete basis set CBS-QB3 level of electronic structure theory using the Gaussian 16 suite of programs (Frisch et al., 2016)). Although this is only 24% of the available kinetic energy, atomization is likely to occur through successive collisions with air molecules i.e. PO<sub>2</sub> + M (=N<sub>2</sub> or O<sub>2</sub>) → PO + O, followed by PO + M → P + O. If the first collision is inelastic and the PO<sub>2</sub> recoils with just enough internal energy to dissociate, then the resulting PO fragment will have a velocity of  $6.3 \text{ km s}^{-1}$ . Although its kinetic energy of  $932 \text{ kJ mol}^{-1}$  is larger than the P–O bond energy of  $593 \text{ kJ mol}^{-1}$ , dissociation of PO on the next collision with an air molecule would require 64% of the collision energy to go into internal vibrational excitation of PO, which is a relatively high fraction and thus unlikely, because the energy should be distributed between translational, rotational and vibrational modes of PO and M. In contrast, if the infall velocity of the parent meteoroid were  $20 \text{ km s}^{-1}$ , then only 21% of the PO's collision energy would be required to

dissociate it. At the maximum possible infall velocity of  $72 \text{ km s}^{-1}$ , only 1.6% of the PO collision energy would be needed, and so dissociation to P would be very likely.

These simple estimates indicate that ablated PO<sub>2</sub> will very likely always dissociate to PO, and this in turn will probably dissociate to P if the infall velocity is  $20 \text{ km s}^{-1}$  or higher. Directly ablated PO will very likely dissociate to P. However, we have recently measured the rate coefficient for the reaction



to be  $1.2 \times 10^{-13} \text{ cm}^3 \text{ molecule}^{-1} \text{ s}^{-1}$  at 200 K (Douglas et al., 2019). Hence, any P that is produced following ablation of PO<sub>2</sub> (or PO) will be oxidized to PO in around 0.5 s at 90 km in the terrestrial atmosphere. Lastly, the formation of ionized phosphorus species through hyperthermal collisions should be limited because the ionization potentials of PO and PO<sub>2</sub> are relatively large (compared to metals such as Na and Fe), being 8.4 and 10.5 eV, respectively (Lias and Bartmess, 2018).

## 4. Summary and conclusions

The MASI experiments with  $\mu\text{m}$ -size meteoritic particles demonstrate that phosphorus is moderately volatile and ablates earlier than refractory Ca. K-edge (XANES) spectroscopy on IDPs shows that P is mainly found in phosphate-like domains. The CABMOD ablation model satisfactorily reproduces the experimental ablation profiles using a thermodynamic treatment for phosphate based on a Regular Solution, which is extensively used in the metallurgy and glassmaking industries to describe the distribution of phosphorus between the molten steel and the multicomponent slag. The MASI experiments show that the ablation of phosphorus occurs at a relatively low temperature of around 2200 K.

CABMOD was then combined with the Zodiacal Cloud Model (ZoDy) to estimate that the global influx of phosphorus into the upper atmospheres of Earth, Mars, and Venus are  $0.017 \text{ t d}^{-1}$ ,  $1.15 \times 10^{-3} \text{ t d}^{-1}$ , and  $0.024 \text{ t d}^{-1}$ , respectively, with overall ablation efficiencies similar to Ni. The modelling results show that the speciation of the injected phosphorus depends on the oxygen fugacity, and that for a typical CI-composition ~86% of the phosphorus will ablate as PO<sub>2</sub>, which is then likely to be dissociated to PO through hyperthermal collisions with air molecules. The injection profiles of P species calculated in the present study can now be used in atmospheric chemistry models to determine the fraction of ablated P that reaches the surface as phosphate and phosphite.

## Declaration of competing interest

The authors declare that they have no known competing financial interests or personal relationships that could have appeared to influence the work reported in this paper.

## CRedit authorship contribution statement

**Juan Diego Carrillo-Sánchez:** Formal analysis, Methodology, Software, Data curation, Writing - original draft, Writing - review & editing. **David L. Bones:** Methodology, Formal analysis, Writing - original draft, Writing - review & editing. **Kevin M. Douglas:** Methodology, Formal analysis, Writing - original draft, Writing - review & editing. **George J. Flynn:** Funding acquisition, Conceptualization, Methodology, Supervision, Writing - original draft. **Sue Wirick:** Methodology, Formal analysis. **Bruce Fegley:** Methodology. **Tohru Araki:** Methodology, Formal analysis. **Burkhard Kaulich:** Methodology. **John M.C. Plane:** Funding acquisition, Conceptualization, Writing - review & editing.

## Acknowledgments

This work is supported by the UK Science and Technology Facilities Council (grant number ST/P000517/1). The synchrotron work was

supported by the DIAMOND-University of Leeds Collaboration. G.J.F is supported by NASA Emerging Worlds grant NNX19AE59G. B.F. was supported by Grant NSF-AST 1517541. The MASI data and CABMOD output are archived at the Leeds University PETAL (PetaByte Environmental Tape Archive and Library; <http://www.see.leeds.ac.uk/business-and-consultation/facilities/petabyte-environmental-tape-archive-and-library-petal/>) and are available upon request to JMCP.

## Appendix A. Supplementary data

Supplementary data to this article can be found online at <https://doi.org/10.1016/j.pss.2020.104926>.

## References

- Adcock, C.T., et al., 2017. Shock-transformation of whitlockite to merrillite and the implications for meteoritic phosphate. *Nat. Commun.* 8, 8.
- Ade, P.A.R., et al., 2014. Planck 2013 results. XIV. Zodiacal emission. *Astron. Astrophys.* 571 art. no.: A14.
- Armstrong, J.T., Elgoresy, A., Wasserburg, G.J., 1985. Willy - a prize noble ur-fremdling - its history and implications for the formation of fremdlinge and cai. *Geochem. Cosmochim. Acta* 49, 1001–1022.
- Ban-Ya, S., 1993. Mathematical expression of Slag metal reactions in steelmaking process by quadratic formalism based on the Regular Solution Model. *ISIJ Int.* 33, 2–11.
- Ban-Ya, S., Hino, M., Sato, A., Terayama, O., 1991. O, P, and S distribution equilibria between liquid-iron and CaO-Al<sub>2</sub>O<sub>3</sub>-Fe<sub>2</sub>O<sub>3</sub> slag saturated with CaO. *Tetsu-to-Hagane (Journal of the Iron and Steel Institute of Japan)* 77, 361–368.
- Bones, D.L., Carrillo-Sánchez, J.D., Kulak, A.N., Plane, J.M.C., 2019. Ablation of Ni from micrometeoroids in the upper atmosphere: experimental and computer simulations and implications for Fe ablation. *Planet. Space Sci.* 179 art. no.: 104725.
- Bones, D.L., et al., 2016. A novel instrument to measure differential ablation of meteorite samples and proxies: the Meteoric Ablation Simulator (MASI). *Rev. Sci. Instrum.* 87 art. no.: 094504.
- Bones, D.L., Gómez Martín, J.C., Carrillo Sánchez, J.D., Dobson, A.J., Plane, J.M.C., 2018. Characterization of the extraterrestrial magnesium source in the atmosphere using a meteoric ablation simulator. *Geophys. Res. Lett.* 45, 7765–7771.
- Brandes, J.A., Ingall, E., Paterson, D., 2007. Characterization of minerals and organic phosphorus species in marine sediments using soft X-ray fluorescence spectromicroscopy. *Mar. Chem.* 103, 250–265.
- Bryant, D.E., et al., 2013. Hydrothermal modification of the Sikhote-Alin iron meteorite under low pH geothermal environments. A plausibly prebiotic route to activated phosphorus on the early Earth. *Geochem. Cosmochim. Acta* 109, 90–112.
- Buchwald, V.F., 1984. Chapter 5: phosphate minerals in meteorites and lunar rocks. In: Nriagu, J.O., Moore, P.B. (Eds.), *Phosphate Minerals*. Springer, Berlin, pp. 199–214.
- Campbell, A.J., Simon, S.B., Humayun, M., Grossman, L., 2003. Chemical evolution of metal in refractory inclusions in CV3 chondrites. *Geochem. Cosmochim. Acta* 67, 3119–3134.
- Carrillo-Sánchez, J.D., et al., 2020. Cosmic dust fluxes in the atmospheres of earth, Mars, and Venus. *Icarus* 335 art. no.: 113395.
- Carrillo-Sánchez, J.D., Nesvorný, D., Pokorný, P., Janches, D., Plane, J.M.C., 2016. Sources of cosmic dust in the Earth's atmosphere. *Geophys. Res. Lett.* 43, 11979–11986.
- Chase, M.W., Davies, C.A., Downey Jr., J.R., Frurip, D.J., McDonald, R.A., Syverud, A.N., 1985. *JANAF Thermodynamic Tables*. *J. Phys. Chem. Ref. Data* vol. 14 third ed.
- Chen, C.L., Zhang, L., Lehmann, J., 2013. Thermodynamic modelling of phosphorus in steelmaking slags. *High Temp. Mater. Process.* 32, 237–246.
- Clarke, R.S.J., Jarosewich, E., Mason, B., Nelem, J., Gómez, M., Hyde, J.R., 1971. The Allende, Mexico, Meteorite Shower. *The Smithsonian Contributions to the Earth Sciences*, Washington.
- Consolmagno, G.J., Britt, D.T., Macke, R.J., 2008. The significance of meteorite density and porosity. *Chemie Der Erde-Geochemistry* 68, 1–29.
- Crismani, M.M.J., et al., 2018. The impact of comet siding spring's meteors on the martian atmosphere and ionosphere. *J. Geophys. Res. Planets* 123, 2613–2627.
- Douglas, K.M., Blitz, M.A., Mangan, T.P., Plane, J.M.C., 2019. Experimental study of the removal of ground- and excited-state phosphorus atoms by atmospherically relevant species. *J. Phys. Chem. A* 123, 9469–9478.
- Ebihara, M., Honda, M., 1987. Rare earth elements in Ca phosphates of Allende carbonaceous chondrite. *Meteoritics* 22, 179–190.
- Fegley, B.J., Cameron, A.G.W., 1987. A vaporization model for Iron Silicate fractionation in the Mercury protoplanet. *Earth Planet Sci. Lett.* 82, 207–222.
- Fixsen, D.J., Dwek, E., 2002. The zodiacal emission spectrum as determined by COBE and its implications. *Astrophys. J.* 578, 1009–1014.
- Flynn, G.J., Keller, L.P., Feser, M., Wirick, S., Jacobsen, C., 2003. The origin of organic matter in the solar system: evidence from the interplanetary dust particles. *Geochem. Cosmochim. Acta* 67, 4791–4806.
- Flynn, G.J., Northrup, P., Wirick, S., 2015. P, S, and K K-edge x-ray absorption near-edge structure (XANES) spectroscopy of large cluster IDPs. In: 46th Lunar and Planetary Science Conference. Universities Space Research Association, The Woodlands, Texas, p. 1260. LPI Contribution No. 1832.
- Flynn, G.J., Wirick, S., Keller, L.P., 2013. A carbon-XANES study of IDP organic diversity: evidence for multiple sources of early solar system organic matter. *Meteoritics Planet Sci.* 48, A126-A126.
- Flynn, G.J., Wirick, S., Northrup, P., 2019a. P speciation in large, cluster interplanetary dust particles. 50th Lunar and Planetary Science Conference. Lunar and Planetary Institute, Houston. Abstract #1403.
- Flynn, G.J., Wirick, S., Northrup, P., 2019b. Phosphorus speciation in primitive interplanetary dust: clues to grain formation in the solar protoplanetary disk. *Meteoritics Planet Sci.* 54. LPI Contrib. No.2157.
- Frisch, M.J., et al., 2016. *Gaussian 16*, Revision B.01. Gaussian, Inc., Wallingford, CT, USA.
- Fuchs, L.H., 1962. Occurrence of whitlockite in chondritic meteorites. *Science* 137, 425–426.
- Giguet-Covex, C., et al., 2013. XANES spectroscopy as a tool to trace phosphorus transformation during soil genesis and mountain ecosystem development from lake sediments. *Geochem. Cosmochim. Acta* 118, 129–147.
- Gingerich, K.A., 1969. Gaseous phosphorus compounds. 3. Mass spectrometric study of reaction between diatomic nitrogen and phosphorus vapor and dissociation energy of phosphorus mononitride and diatomic phosphorus. *J. Phys. Chem.* 73, 2734–2741.
- Glushko, V.P., et al., 1978-1982. *Thermodynamic Properties of Individual Substances*. High Temperature Institute, Moscow.
- Gómez-Martín, J.C., et al., 2017. Novel experimental simulations of the atmospheric injection of meteoric metals. *Astrophys. J.* 836 art. no.: 212.
- Grosvenor, A.P., Wik, S.D., Cavell, R.G., Mar, A., 2005. Examination of the bonding in binary transition-metal monophosphides MP (M = Cr, Mn, Fe, Co) by X-ray photoelectron spectroscopy. *Inorg. Chem.* 44, 8988–8998.
- Grün, E., Krüger, H., Srama, R., 2019. The dawn of dust astronomy. *Space Sci. Rev.* 215, 46.
- Gu, T.T., Fei, Y.W., Wu, X., Qin, S., 2014. High-pressure behavior of Fe<sub>2</sub>P and the role of phosphorus in planetary cores. *Earth Planet Sci. Lett.* 390, 296–303.
- Hastie, J.W., Bonnell, D.W., 1985. A predictive phase-equilibrium model for multicomponent oxide mixtures. 2. Oxides of Na-K-Ca-Mg-Al-Si. *High Temp. Sci.* 19, 275–306.
- Hastie, J.W., Bonnell, D.W., 1986. A predictive thermodynamic model of oxide and halide glass phase-equilibria. *J. Non-Cryst. Solids* 84, 151–158.
- Hastie, J.W., Bonnell, D.W., Plante, E.R., Horton, W.S., 1984. Thermodynamic activity and vapor pressure models for silicate systems including coal slags. In: Ribeiro da Silva, M.A.V. (Ed.), *Thermochemistry and its Applications to Chemical and Biochemical Systems: the Thermochemistry of Molecules, Ionic Species and Free Radicals in Relation to the Understanding of Chemical and Biochemical Systems*. Springer Netherlands, Dordrecht, pp. 235–251.
- Hastie, J.W., Plante, E.R., Bonnell, D.W., 1982. Alkali vapor transport in coal conversion and combustion systems. *ACS (Am. Chem. Soc.) Symp. Ser.* 179, 543–600.
- Herzberg, G., 1945. *Spectra of Diatomic Molecules*. Van Nostrand Reinhold Company, New York, USA.
- Hultgren, R., Desai, P.D., Hawkins, D.T., Gleiser, M., Kelley, K.K., 1973. Selected values of the thermodynamic properties of the elements. In: A. S. F. M. International, (Ed.), *Metals Park, Ohio, USA*, p. 371.
- Hutchinson, R., 2007. *Meteorites: A Petrologic, Chemical and Isotopic Synthesis*. Cambridge University Press, Cambridge, UK.
- Ingall, E.D., et al., 2011. Phosphorus K-edge XANES spectroscopy of mineral standards. *J. Synchrotron Radiat.* 18, 189–197.
- Ishii, H.A., et al., 2008. Comparison of comet 81P/Wild 2 dust with interplanetary dust from comets. *Science* 319, 447–450.
- Janches, D., et al., 2017. Radar detectability studies of slow and small zodiacal dust Cloud particles. III. The role of sodium and the Head echo size on the probability of detection. *Astrophys. J.* 843 art. no. 1.
- Jung, I.H., Hudon, P., 2012. Thermodynamic assessment of P<sub>2</sub>O<sub>5</sub>. *J. Am. Ceram. Soc.* 95, 3665–3672.
- Jung, I.H., Hudon, P., Kim, W.Y., van Ende, M.A., Rahman, M., Curiel, G.G., 2013. Thermodynamic database of P<sub>2</sub>O<sub>5</sub>-containing oxide systems for the dephosphorization process in steelmaking. *High Temp. Mater. Process.* 32, 247–254.
- Khadhraoui, S., Hack, K., Jantzen, T., Odenthal, H.J., 2019. Study of the state of industrial P<sub>2</sub>O<sub>5</sub>-containing slags relevant to steelmaking processes based on a new thermodynamic database developed for CaO-FeO<sub>x</sub>-P<sub>2</sub>O<sub>5</sub>-SiO<sub>2</sub>-MnO-MgO-Al<sub>2</sub>O<sub>3</sub> slags - Part I: ternary and lower order systems. *Steel Res. Int.* 90, 16.
- Kim, B., Gautier, M., Rivard, C., Sanglar, C., Michel, P., Gourdon, R., 2015a. Effect of aging on phosphorus speciation in surface deposit of a vertical flow constructed wetland. *Environ. Sci. Technol.* 49, 4903–4910.
- Kim, B., Gautier, M., Rivard, C., Sanglar, C., Michel, P., Gourdon, R., 2015b. Effect of aging on phosphorus speciation in surface deposit of a vertical flow constructed wetland. *Environ. Sci. Technol.* 49, 4903–4910.
- Küper, G., et al., 1992. Phosphorus K shell photoabsorption spectra of the oxides P<sub>4</sub>O<sub>6</sub>, P<sub>4</sub>O<sub>10</sub>, P(C<sub>6</sub>H<sub>5</sub>O)<sub>3</sub> and PO(C<sub>6</sub>H<sub>5</sub>O)<sub>2</sub>. *Chem. Phys.* 165, 405–414.
- Küper, G., Hormes, J., 1994. In-situ X-ray absorption spectroscopy at the K-edge of red phosphorus in polyamide 6,6 during a thermo-oxidative degradation. *Macromol. Chem. Phys.* 195, 1741–1753.
- Li, B., Li, L., Guo, H.J., Guo, J., Duan, S.C., Sun, W.X., 2019. A phosphorus distribution prediction model for CaO-SiO<sub>2</sub>-MgO-FeO-Fe<sub>2</sub>O<sub>3</sub>-Al<sub>2</sub>O<sub>3</sub>-P<sub>2</sub>O<sub>5</sub> slags based on the IMCT. *Ironmak. Steelmak.* <https://doi.org/10.1080/03019233.2019.1608421>.
- Li, W., Joshi, S.R., Hou, G., Burdige, D.J., Sparks, D.L., Jaisi, D.P., 2015. Characterizing phosphorus speciation of Chesapeake Bay sediments using chemical extraction, <sup>31</sup>P NMR, and X-ray absorption fine structure spectroscopy. *Environ. Sci. Technol.* 49, 203–211.
- Lias, S.G., Bartmess, J.E., 2018. *Gas-phase Ion Thermochemistry - NIST Standard Reference Database Number 69*. National Institute of Standards and Technology (NIST), Gaithersburg, USA.
- Lodders, K., 2003. Solar system abundances and condensation temperatures of the elements. *Astrophys. J.* 591, 1220–1247.

- Lodders, K., Fegley Jr., B., 2011. Chemistry of the Solar System. Royal Society of Chemistry, Cambridge, UK.
- Maciá, E., 2005. The role of phosphorus in chemical evolution. *Chem. Soc. Rev.* 34, 691–701.
- Maurette, M., et al., 1991. A collection of diverse micrometeorites recovered from 100 tonnes of Antarctic blue ice. *Nature* 351, 44–47.
- Nesvorný, D., Janches, D., Vokrouhlický, D., Pokorný, P., Bottke, W.F., Jenniskens, P., 2011. Dynamical model for the zodiacal Cloud and sporadic meteors. *Astrophys. J.* 743, 129–144.
- Nesvorný, D., Jenniskens, P., Levison, H.F., Bottke, W.F., Vokrouhlický, D., Gounelle, M., 2010. Cometary origin of the zodiacal Cloud and carbonaceous micrometeorites. Implications for hot debris disks. *Astrophys. J.* 713, 816–836.
- Olette, M., Ancey-Moret, M.F., 1963. Variation of the free energy of formation of oxides and nitrides with temperature. Establishment of the diagrams and examples of application. *Rev. Métall.* 60, 569–581.
- Pasek, M.A., 2008. Rethinking early Earth phosphorus geochemistry. *Proc. Natl. Acad. Sci.* 105, 853–858.
- Pasek, M.A., 2015. Phosphorus as a lunar volatile. *Icarus* 255, 18–23.
- Pasek, M.A., Gull, M., Herschy, B., 2017. Phosphorylation on the early earth. *Chem. Geol.* 475, 149–170.
- Pellinen-Wannberg, A., Haggstrom, I., Carrillo Sánchez, J.D., Plane, J.M.C., Westman, A., 2014. Strong E region ionization caused by the 1767 trail during the 2002 Leonids. *J. Geophys. Res.* 119, 7880–7888.
- Pirim, C., Pasek, M.A., Sokolov, D.A., Sidorov, A.N., Gann, R.D., Orlando, T.M., 2014. Investigation of schreibersite and intrinsic oxidation products from Sikhote-Alin, Seymchan, and Odessa meteorites and Fe<sub>3</sub>P and Fe<sub>2</sub>NiP synthetic surrogates. *Geochem. Cosmochim. Acta* 140, 259–274.
- Plane, J.M.C., et al., 2017. Impacts of cosmic dust on planetary atmospheres and surfaces. *Space Sci. Rev.* 214, 23.
- Redfield, A.C., 1958. The biological control of chemical factors in the environment. *Am. Sci.* 46, 205–221.
- Richardson, F.D., Jeffes, J.H.E., 1948. The thermodynamics of substances of interest in iron and steel making from 0°C to 2400°C. *J. Iron Steel Inst.* 160, 261–270.
- Rivard, C., Lanson, B., Cotte, M., 2016. Phosphorus speciation and micro-scale spatial distribution in North-American temperate agricultural soils from micro X-ray fluorescence and X-ray absorption near-edge spectroscopy. *Plant Soil* 401, 7–22.
- Robie, R.A., Hemingway, B.S., Fisher, J.R., 1979. Thermodynamic Properties of Minerals and Related Substances at 298.15 K and 1 Bar (10<sup>5</sup> Pascals) Pressure and at Higher Temperatures. U.S. Geological Survey Bulletin, Washington D.C., pp. 331–332.
- Rojkovic, I., Siman, P., Porubcan, V., 1997. Rumanova H5 chondrite, Slovakia. *Meteoritics Planet Sci.* 32, A151–A153.
- Rubin, A.E., 1991. Euhedral awaruite in the allende meteorite - implications for the origin of awaruite-bearing and magnetite-bearing nodules in CV3 chondrites. *Am. Mineral.* 76, 1356–1362.
- Sausa, R.C., Miziolek, A.W., Long, S.R., 1986. State distributions, quenching, and reaction of the PO radical generated in excimer laser photofragmentation of dimethyl methylphosphonate. *J. Phys. Chem.* 90, 3994–3998.
- Schaefer, L., Fegley, B., 2005. Application of an equilibrium vaporization model to the ablation of chondritic and achondritic meteoroids. *Earth Moon Planets* 95, 413–423.
- Schlesinger, M.E., 2002. The thermodynamic properties of phosphorus and solid binary phosphides. *Chem. Rev.* 102, 4267–4301.
- Schneider, N.M., et al., 2015. MAVEN IUVS observations of the aftermath of the Comet Siding Spring meteor shower on Mars. *Geophys. Res. Lett.* 42, 4755–4761.
- Schwartz, A.W., 2006. Phosphorus in prebiotic chemistry. *Phil. Trans. Roy. Soc. London Ser. B* 361, 1743–1749.
- Stull, D.R., Prophet, H., 1971. JANAF Thermochemical Tables. U.S. Dept. of Commerce, National Bureau of Standards, Washington, D.C.
- Suito, H., Inoue, R., 1982. Effect of calcium-fluoride on phosphorus distribution between MgO saturated slags of the system CaO-MgO-FeO<sub>x</sub>-SiO<sub>2</sub> and liquid iron. *Trans. Iron Steel Inst. Jpn.* 22, 869–877.
- Suito, H., Inoue, R., Takada, M., 1981. Phosphorus distribution between liquid-iron and MgO saturated slags of the system CaO-MgO-FeO-SiO<sub>2</sub>. *Trans. Iron Steel Inst. Jpn.* 21, 250–259.
- Swarnalingam, N., et al., 2019. Modeling the altitude distribution of meteor Head Echoes observed with HPLA radars - implications on the radar detectability of meteoroid populations. *Astrophys. J.* 157, 179–193.
- Swartzendruber, L.J., Itkin, V.P., Alcock, C.B., 1991. The Fe-Ni (iron-nickel) system. *J. Phase Equil.* 12, 288–312.
- Turkdogan, E.T., 2000. Assessment of P<sub>2</sub>O<sub>5</sub> activity coefficients in molten slags. *ISIJ Int.* 40, 964–970.
- Turkdogan, E.T., Pearson, J., 1953. Part III phosphorus pentoxide. *J. Iron Steel Inst.* 175, 398–401.
- Vondrak, T., Plane, J.M.C., Broadley, S., Janches, D., 2008. A chemical model of meteoric ablation. *Atmos. Chem. Phys.* 8, 7015–7031.
- Ward, D., Bischoff, A., Roszjar, J., Berndt, J., Whitehouse, M.J., 2017. Trace element inventory of meteoritic Ca-phosphates. *Am. Mineral.* 102, 1856–1880.
- Wirick, S., Flynn, G.J., Jacobsen, C., Keller, L.P., 2006. Organics in the Murchison Meteorite Using Carbon XANES Spectroscopy. 37th Lunar and Planetary Science Conference. Lunar and Planetary Institute, Houston. Abstract #1418.
- Wlotzka, F., 1976. Phosphates in the Allende carbonaceous chondrite. *Meteoritics* 11, 393–394.
- Yang, X.M., Li, J.Y., Chai, G.M., Duan, D.P., Zhang, J., 2016. Critical assessment of P<sub>2</sub>O<sub>5</sub> activity coefficients in CaO-based slags during dephosphorization process of iron-based melts. *Metall. Mater. Trans. B* 47, 2330–2346.
- Yang, X.M., Li, J.Y., Zhang, M., Chai, G.M., Duan, D.P., Zhang, J., 2018. Coupling relationship between dephosphorisation and desulphurisation abilities or potentials for CaO-FeO-Fe<sub>2</sub>O<sub>3</sub>-Al<sub>2</sub>O<sub>3</sub>-P<sub>2</sub>O<sub>5</sub> slags over a large variation range of slag oxidation ability during secondary refining process of molten steel. *Ironmak. Steelmak.* 45, 25–43.
- Zhai, S., Akaogi, M., Kojitani, H., Xue, W., Ito, E., 2014. Thermodynamic investigation on β- and γ-Ca<sub>3</sub>(PO<sub>4</sub>)<sub>2</sub> and the phase equilibria. *Phys. Earth Planet. In.* 228, 144–149.